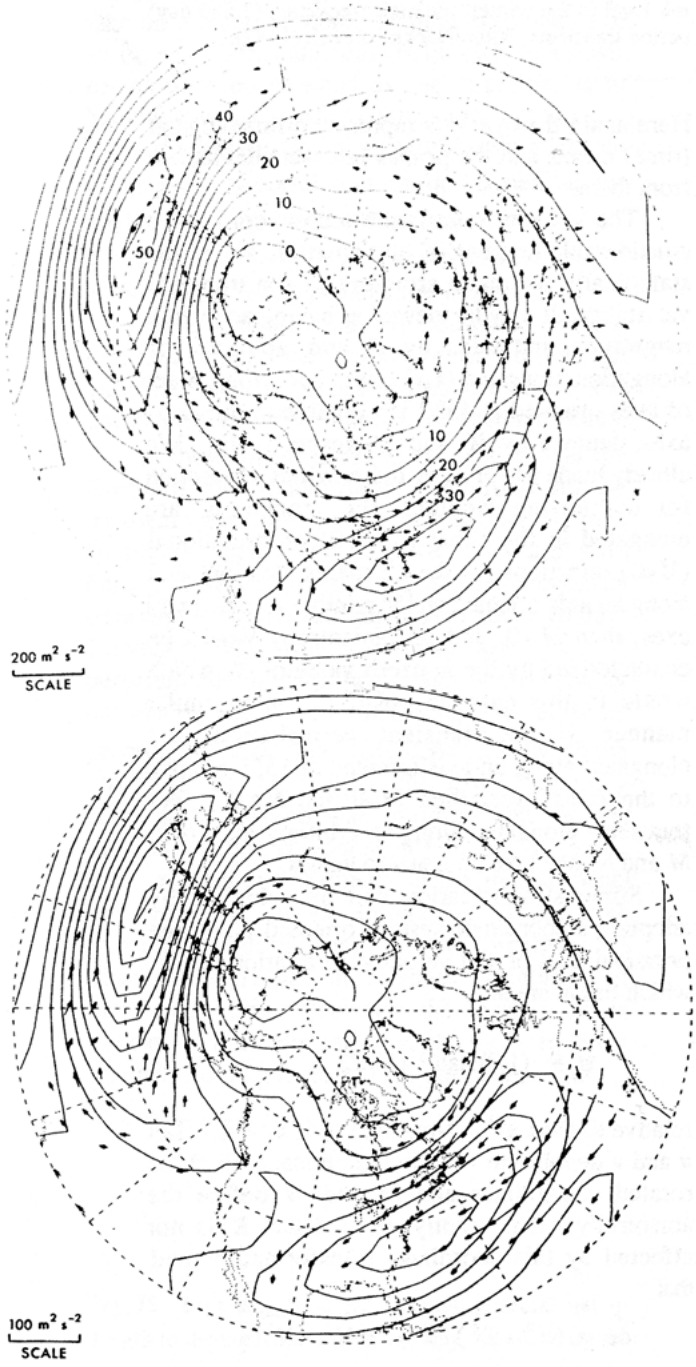

Fig.13 As in Fig. 12, but based on an extended perpetual winter simulation with the *M* version of the same GFDL general circulation model. (a) unfiltered data, (b) monthly mean data. After Wallace and Lau (1985)

2.3 Anisotropy of the observed transients

The observed transient variability in the horizontal wind field exhibits a substantial amount of anisotropy, particularly in time-filtered data. For example, Fig. 14 shows distributions of $\overline{u'^2}$, $\overline{v'^2}$, and $\overline{u'v'}$ at the 500mb level for the high frequency (2.5–6 day period) fluctuations during the winter months. The fact that all three fields exhibit a substantial amount of structure and that $\overline{u'v'}$ is nonzero is, in itself, evidence of anisotropy of the high frequency transients. In addition, it is interesting to note that $\overline{u'^2}$ and $\overline{v'^2}$ exhibit contrasting patterns over the oceanic sectors; the former being characterized by dumbell shaped features with maxima near 30° and 50°N and the latter by elongated maxima along 40°N. It is also notable that $\overline{u'^2} << \overline{v'^2}$, which indicates that the high frequency features on synoptic charts must tend to be elongated in the meridional direction, consistent with the modeling results presented in the previous subsections. The bean shape noted in connection with the high frequency transients in Fig. 10 is implicit in the dipole pattern in the momentum flux in the lower panel.

Hence, distinct patterns are evident in the distributions of $\overline{u'^2}$, $\overline{v'^2}$, and $\overline{u'v'}$ presented in the three panels of Figure 14, and the three distributions, taken together, convey a great deal of useful information concerning the anisotropy of the transients. We will find it most convenient to extract this information, not from the scalar fields of the variance and covariance themselves, but from tensor and vectorial representations of them, which we will now proceed to explain.

Following the formalism developed in Hoskins et al., (1983) the horizontal velocity correlation tensor can be divided into isotropic and anisotropic (trace free) components

$$\begin{vmatrix} \overline{u'^2} & \overline{u'v'} \\ \overline{u'v'} & \overline{v'^2} \end{vmatrix} \quad \begin{vmatrix} K & 0 \\ 0 & K \end{vmatrix} \quad \begin{vmatrix} M & N \\ N & -M \end{vmatrix}$$

where $K \equiv (\overline{u'^2} + \overline{v'^2})/2$

$M \equiv (\overline{u'^2} - \overline{v'^2})/2$, and $N \equiv \overline{u'v'}$

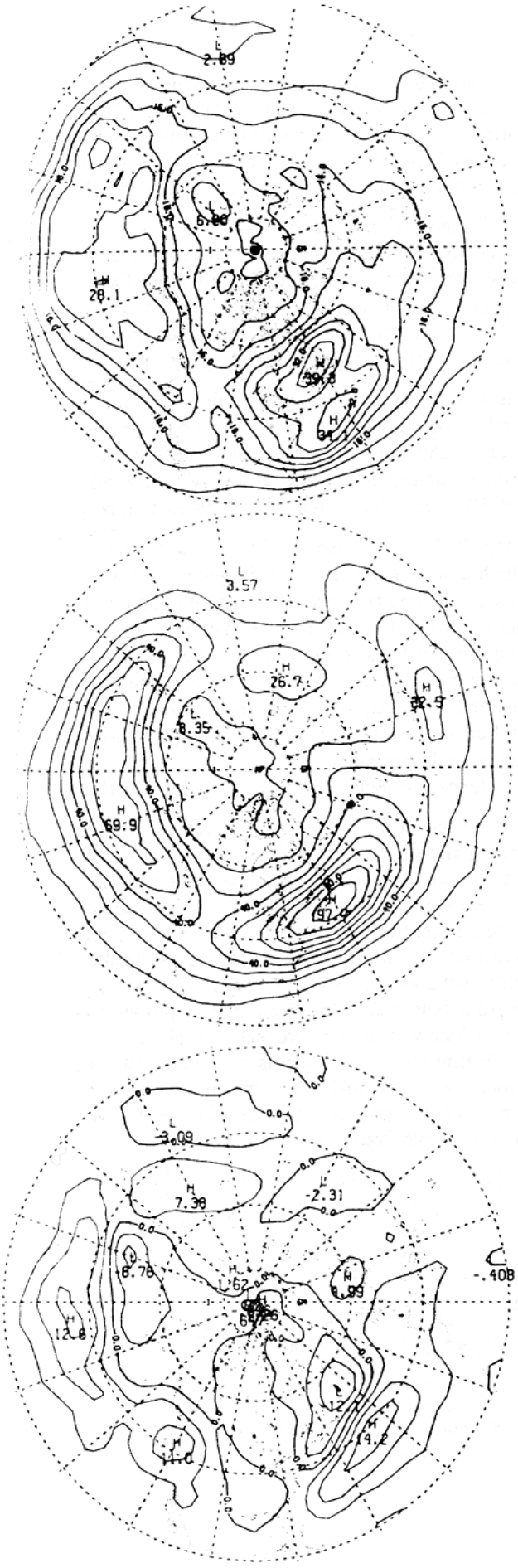

Fig. 14 Temporal standard deviation of the observed *(upper panel)* zonal and *(middle panel)* meridional wind component and *(lower panel)* $u'v'$ at the 500 mb level in the wintertime high frequency (2.5–6 day) period transients. After Blackmon et al. (1977).

Here again the overbars represent climatological (time) means and the primes represent deviations from them.

The velocity correlation tensor conveys a considerable amount of information about the statistically averaged structure of the transient variability. It may be viewed as having an overall magnitude, indicated by K, and amounts of elongation along the (x,y) axes, and along a set of axes oriented at 45°/135° relative to the (x,y) axes, denoted by M and N, respectively. We already made use of M in the previous subsection for diagnosing whether the transients are elongated in the zonal ($M > 0$) or meridional ($M<0$) directions. If the transients are elongated along an axis oriented at 45° relative to the (x,y) axes, then $M=0$, and the anisotropy would be characterized by the nonzero value of N, which would in this case be positive. In a similar manner, if the transient perturbations are elongated along an axis oriented at 135° relative to the (x,y) axes, then $M=0$ and $N<0$. For transients elongated along an arbitrary axis, both M and N may take on nonzero values.

Some simplification can be achieved by adopting a coordinate system oriented along the principal axes of the velocity correlation tensor, which lies at angle

$$\psi \equiv (1/2)\ \tan^{-1}(N/M)$$

relative to the x axis. Note that $0 < \psi < \pi$. Let u and v denote the velocity components in these rotated coordinates and M and N define the anisotropy. It is readily verified that K is not affected by this coordinate transformation and that

$$\hat{M} \equiv (\overline{u'^2} - \overline{v'^2})/2 = \sqrt{M^2 + N^2}$$

$$\text{and} \quad N = 0.$$

Hence, in these rotated coordinates, M and ψ convey all the essential information about the anisotropy of the horizontal wind field. In addition, it is useful to define

$$\alpha \equiv -M / K$$

as a measure of the normalized anisotropy. It is evident that this *coefficient of anisotropy* may take on a range of values from zero to one. For an isotropic horizontal wind field it would vanish; for motions constrained to one direction, as in Kelvin waves, it would assume a value of unity.

An ellipse provides a useful visual analogue of the velocity correlation tensor. ψ defines the angle of its major axis and α is a measure of its ellipticity; for α=0 the ellipse degenerates into a circle and for α=1 it degenerates into a slit.

These statistics can be calculated for the transient variability as a whole or for the transient variablility in any particular frequency band that one can isolate through the use of temporal filters. Fig. 15 shows the distribution of α and ψ over the Northern Hemisphere during wintertime for the transient variability as a whole (top), for the high frequency transients that we associate with baroclinic waves (middle) and for low-frequency transients with periods longer than about 10 days (lower). The line segments are oriented perpendicular to the principal axis of the velocity correlation tensor, and their length scaled to be proportional to α. The sharp contrast between the structure of the high and low frequency fluctuations, which was pointed out in the previous section is evident in Fig.15. The east - west oriented line segments in the middle panel are indicative of an elongation of the high frequency fluctuations in the north-south direction, while the north-south orientation of many of the line segments in the lower panel is indicative of an elongation of the low frequency fluctuations in the east-west direction. Not

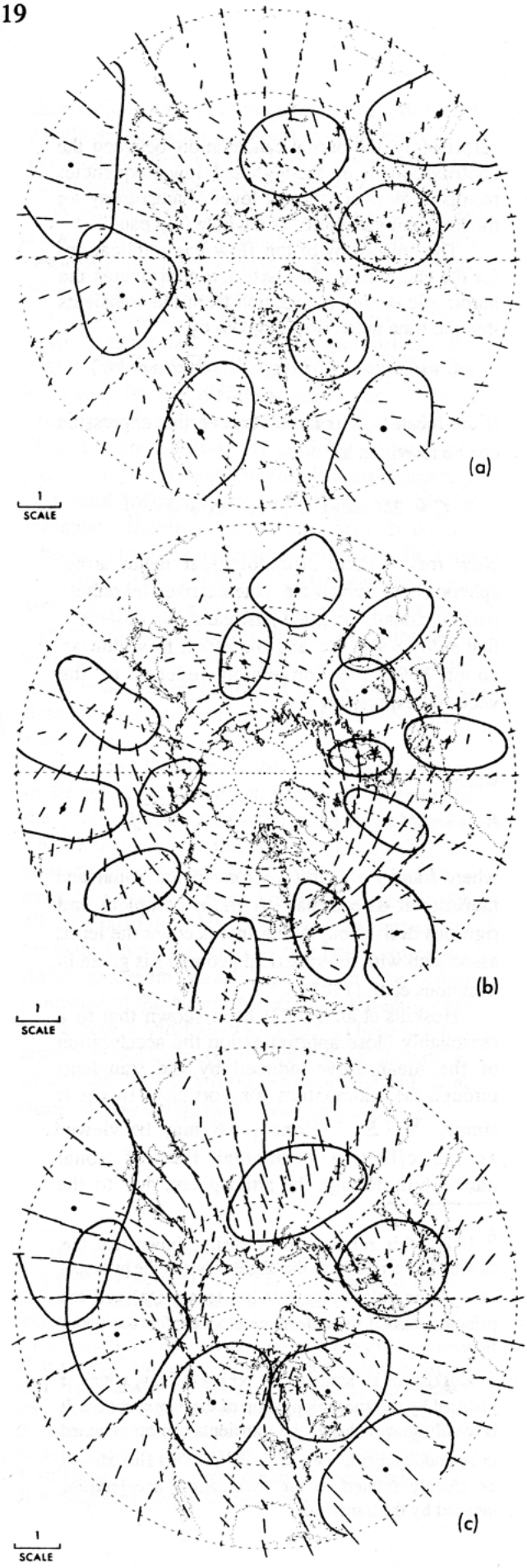

Fig. 15 Line segments are linearly proportional in length to the coefficient of anisotropy, α, and they are oriented perpendicular to the angle ψ, or parallel to the minor axis of the velocity correlation tensor. Based on wintertime 300mb wind statistics, Top panel: all transients. Middle panel: high frequency transients with 2.5-6 day periods. Lower panel: low frequency transients with periods longer than 10 days. After Wallace and Lau (1985).

surprisingly, the partial cancellation between the contributions from the high and low frequencies results in an overall lower level of anisotropy for the transient variability as a whole (top panel).

The anisotropy of the flow has implications for the energetics. In Cartesian coordinates the barotropic energy conversion from the transients into the time mean flow is given by

$$C = -\overline{u'^2}\,\partial\bar{u}/\partial x + \overline{v'^2}\,\partial\bar{v}/\partial y + \overline{u'v'}\,(\partial\bar{v}/\partial x + \partial\bar{u}/\partial y)$$

If the mean flow is nondivergent, this expression can be rewritten as[6]

$$C = 2M\,\partial\bar{u}/\partial x + N\,(\partial\bar{v}/\partial x + \partial\bar{u}/\partial y)$$

Now for realistic climatological mean atmospheric flows, which are characterized by rather narrow, zonally oriented jetstreams, we observe that $\partial\bar{u}/\partial y >> \partial\bar{v}/\partial x$, and therefore, to within an about 10%, the conversion reduces to the vectorial expression

$$C = -\boldsymbol{E} \cdot \nabla \bar{u}$$

where

$$\boldsymbol{E} \equiv [-2M\boldsymbol{i}, -N\boldsymbol{j}] = (\overline{v'^2} - \overline{u'^2})\boldsymbol{i}, -\overline{u'v'}\boldsymbol{j},$$

where $\boldsymbol{i}$ and $\boldsymbol{j}$ are unit vectors in the zonal and meridional directions. A more complete and rigorous derivation, taking into account the terms associated with the spherical geometry is given in Simmons et al. (1983).

Hoskins et al. (1983) have shown that to a reasonably close approximation the acceleration of the mean flow induced by the transients through the momentum (or vorticity) fluxes is simply $\nabla \cdot \boldsymbol{E}$.[7] Hence, $-\boldsymbol{E}$ may be viewed as the effective horizontal flux of zonal momentum through the atmosphere, due to the transients. Like the other transient statistics that we have considered, it may be broken down into contributions from various frequency bands.[8]

$\boldsymbol{E}$ is defined in terms of the same statistics as the velocity correlation tensor but the relation between them is sufficiently complicated to warrant further explanation. Fig. 16 shows the relation between $\boldsymbol{E}$ and the velocity correlation tensor (represented visually in the form of an ellipse as described in the previous section) in a variety of situations. For $M = N = 0$, the ellipse degenerates into a circle, which is indicative of isotropic transients [Panel (g)]. For $M >> N$, $\boldsymbol{E}$ assumes a nearly zonal orientation. For $\overline{v'^2} >> \overline{u'^2}$, $\boldsymbol{E}$ is directed eastward, and since

$$\tan^{-1}(N/2M) \equiv (1/2)\tan^{-1}(N/M),$$

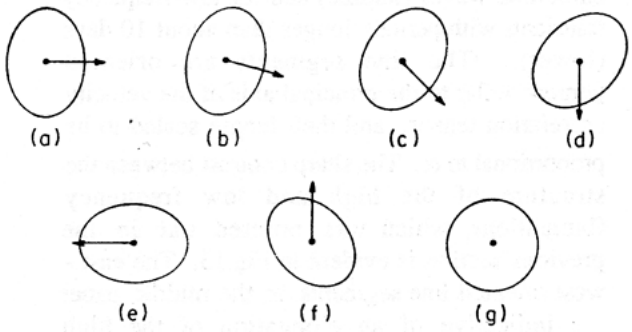

Fig. 16 Schematic illustration of the relationship between the eddy correlation tensor, indicated by the ellipses, and the E vector [calculated with reference to the conventional (x,y) coordinated, indicated by the arrows. (a) $M<0$, $N=0$; (b) $M<0$, $N=-M/2$, (c) $M<0$, $N=-2M$; (d) $M=0$, $N>0$; (e) $M>0$, $N<0$, (g) $M=0$, $N=0$.

[6] Using this relation, it is easily shown that the conversion is related to the angle between the principal axis of the velocity correlation tensor (ψ) and the principal axis if the deformation tensor for the mean flow.

[7] Hoskins et al. assume that Nxx << Nxy, which is justified by the zonal elongation of the stormtracks. It is readily shown that if the transients can be assumed to be nondivergent, $\nabla \cdot \boldsymbol{E} = \overline{v'\zeta'}$. This flux should be closely related to the local zonal acceleration induced by the transients.

[8] Hoskins et al. (1983) have also shown that if the angle between $\boldsymbol{E}$ and the horizontal axis is not too large, $\boldsymbol{E}$ is closely related to the group velocity vector or the flux of "wave action" associated with the transients, and thus has a dual interpretation analogous to the *Eliassen-Palm flux* defined by Edmon et al. (1980). The minus sign in the definition, which is actually rather awkward for the purposes of these lectures, is to make $\boldsymbol{E}$ point in the direction of the group velocity vector. The vertical component of $\boldsymbol{E}$ (directed upward) is directly proportional to the local, poleward heat flux divided by the static stability. Trenberth (1986), Andrews (1983) and Plumb (1985, 1986) have discussed more exact formulations, but they are more complex and more difficult to interpret.

it must be almost coincident with the minor axis of the velocity correlation tensor, as indicated in panel (b). It is evident from Fig.15 (middle panel) that this situation prevails over much of the hemisphere in the case of the high frequency transients. For $M >> N$ and $u'^2 >> v'^2$, $\boldsymbol{E}$ is directed westward and, for the same reason, it almost exactly coincides with the major axis of the velocity correlation tensor, as in Panel (e). This situation is applicable to the low-frequency transients over much of the hemisphere. However, in the more general case, in which N is greater than $M/2$ in absolute value, as in (c) and (d), $\boldsymbol{E}$ will not tend to be parallel to either axis. For example, when $M=0$, $\boldsymbol{E}$ is oriented in the meridional direction, whereas the minor axis of the ellipse is oriented at 45° relative to the zonal axis, as in Panels (d) and (f).

The $\boldsymbol{E}$ vectors[9] in Fig.11, based on monthly mean 200mb wind field for the GCM simulation without mountains or land-sea contrasts, are almost uniformly due westward indicating, as noted previously, an east-west elongation of the low- frequency transients. Upon close inspection (if one has good eyesight) one can detect a slight equatorward component of the vectors, indicative of a poleward flux of zonal momentum. The meridional fluxes are more apparent in the unfiltered 200mb wind field in the *NM* simulation, shown in Fig.12, upper panel. Note that the fluxes are largest along the equatorward flank of the jetstream, where the arrows are directed down the gradient of time-mean zonal wind. In this region the flux of westerly momentum is directed *up* the gradient of zonal wind [i.e., in the opposite sense as the $\boldsymbol{E}$ vectors] so that the barotropic energy conversion C, as we have defined it, is positive, with the transients giving up their kinetic energy to the time-mean zonal flow. This situation is representative of the net effect of baroclinic waves upon the mean flow, which is dominated by later, nonlinear stage of their life-cycle [Simmons and Hoskins (1978), Edmon et al. (1980), Held and Hoskins (1985)].

With the GCM simulations as background, we will now examine the $\boldsymbol{E}$ vectors at the 300mb level, shown in Fig. 17, which is based upon observations for eight winters. The four different panels in the figure represent (a) unfiltered data, (b) high frequency fluctuations associated with conventional baroclinic waves, (c) fluctuations with periods longer than about 10 days, and (d) very low frequency fluctuations which are resolvable in monthly mean data. Further details are given in the figure caption.

The pattern for the unfiltered data is much more complicated than its counterpart for the *NM* GCM simulation [Fig.12]. $\boldsymbol{E}$ vectors are pointing in all different directions. [The corresponding patterns for the M simulation (Fig. 13) are qualitatively similar.] Hence, it is evident that the major mountain ranges exert a profound influence upon the structure of the transient variability during the northern winter. This effect can be understood by noting that the observed time averaged jetstreams are much stronger and more longitudinally localized than they would be in the absence of mountains [e.g., compare Figs. 12 and 13.] We will subsequently argue that these jet structures play a major role in determining the character of the transient variability.

In order to interpret the complicated pattern in the unfiltered data it will be helpful to examine the contributions from various frequency bands. The high-frequency fluctuations [Panel (b)] are characterized by eastward pointing $\boldsymbol{E}$ vectors extending eastward from Japan to Europe in the 40-50° latitude belt. The arrows appear to emanate from two regions: one poleward of the Asian jetstream, near Japan, and the other poleward of the North American jetstream, near Nova Scotia and Newfoundland. These are the regions of strong baroclinic wave development, as evidenced by the strong poleward 850mb heat fluxes shown in Fig.18.[10] We can relate these

[9] Strictly speaking, E is a psuedo-vector, since it is not invariant with respect to rotation of the coordinate system.

[10] Hoskins et al. (1983) associate the poleward heat flux with the vertical (upward) component of the $\boldsymbol{E}$ vector. This interpretation is valid when $M >> N$, which is certainly the case in Panel (b). Hence, the high-frequency transients assume the form of "bundles of $\boldsymbol{E}$ vectors" emanating from the lower troposphere near Japan and Nova Scotia, turning eastward when they reach the upper troposphere and fanning out over the oceans. They can be interpreted as the group velocity vectors associated with baroclinic waves developing in the two major stormtracks and dispersing their energy downstream.

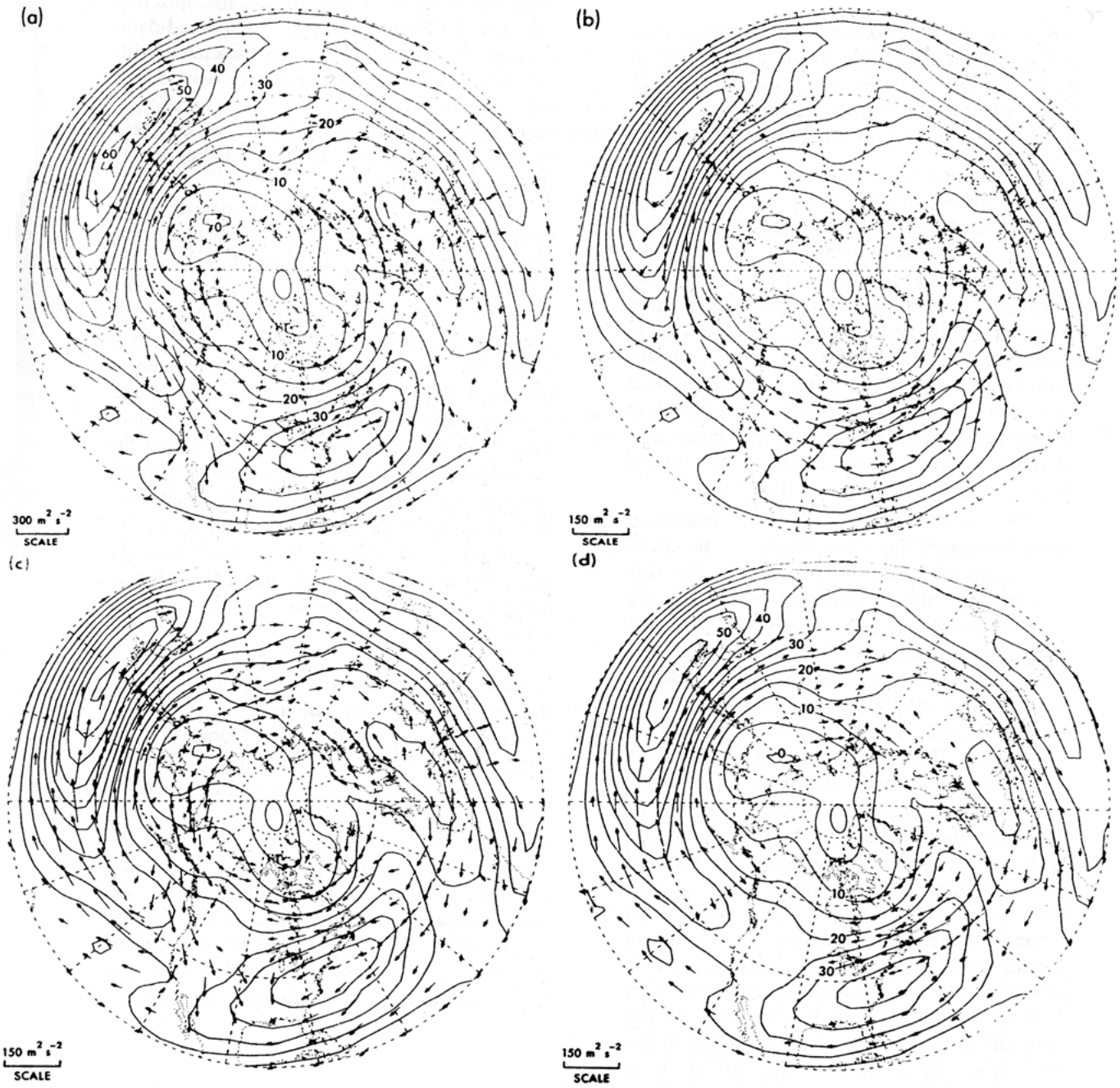

Fig. 17 ***E*** vectors based on observed 300mb wind statistics, superimposed upon the climatological mean zonal wind field, indicated by the contours. (a) for the transients as a whole, (b) for the high frequency transients with 2.5-6 day periods, (c) for low frequency transients with periods longer than about 10 days, and (d) for very low frequency transients resolved by monthly mean data. After Wallace and Lau (1985).

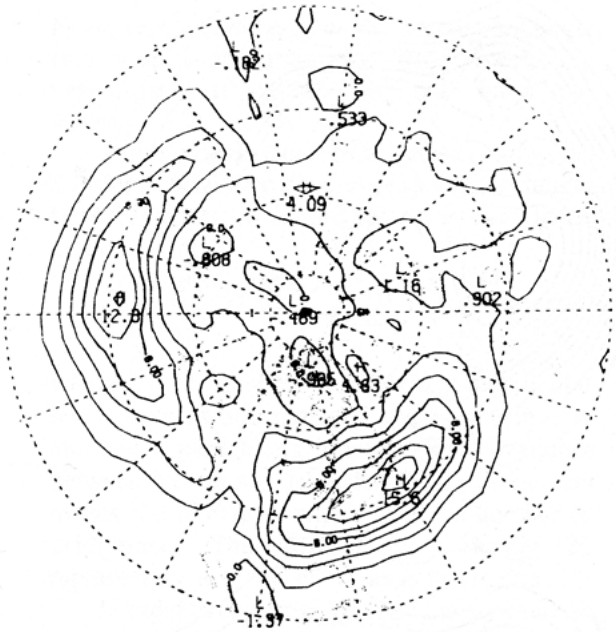

Fig. 18 Observed wintertime poleward heat fluxes during the winter season at the 850mb level by high frequency transients with periods between 2.5 and 6 days. After Blackmon et al. (1977).

features to Fig. 14, which shows the distributions of $\overline{u'^2}$, $\overline{v'^2}$, and $\overline{u'v'}$ for the high frequency fluctuations. Note that in the regions of interest, $\overline{v'^2} >> \overline{u'^2}$, consistent with the eastward pointing arrows in Fig. 17b. The dipole patterns over the mid-oceans in $u'v'$ [Fig. 14, bottom panel] with negative centers to the north and positive centers to the south are consistent with the diffluent pattern of $\boldsymbol{E}$ vectors in Fig. 17b. From the point of view of the energetics, it is evident that the fluxes of zonal momentum (which are in the opposite sense as the arrows) are predominantly up the gradient of u, and therefore the high frequency transients are giving up kinetic energy to the time-mean flow, particularly in the jet exit regions over the mid-oceans.

The structure of the low-frequency transients is most clearly revealed by Fig. 17d. The jet exit regions are again the center of attention, but in this case, the $\boldsymbol{E}$ vectors are pointing westward, indicating that the low frequency transients are gaining kinetic energy via the barotropic energy conversion from the climatological mean flow. This energy conversion is intimately related to the observed zonal elongation of the low-frequency transients in the jet exit regions [Fig.15]. A similar pattern is evident in Panel (c), which also shows bands of southward pointing $\boldsymbol{E}$ vectors over the jet entrance regions over the western United States and North Africa. These vectors are also directed up the gradient of climatological mean zonal wind, indicating a transfer of kinetic energy from the mean flow to the transients. These features are evidently associated with features on synoptic charts which exhibit a pronounced northeast / southwest orientation. The cutoff lows that often develop over these regions during wintertime exhibit such a preferred orientation, as evidenced by the example shown in Fig. 19.

The $\boldsymbol{E}$ vectors based upon unfiltered data, shown in Fig. 17a, exhibit a complicated pattern which contains elements of all the features mentioned above. The equatorward component of the arrows in the jet entrance regions is particularly pronounced, since this behavior appears to be common to all frequency bands.

The features pointed out in Fig. 17 account for all the major maxima and minima in the hemispheric barotropic energy conversion $C = -\boldsymbol{E} \cdot \nabla \bar{u}$, presented by Wallace and Lau (1985) [their Fig. 4]. The low frequencies tend to dominate, so that in the hemispheric mean for the unfiltered data the conversion is predominantly from the climatological mean flow into the transients.

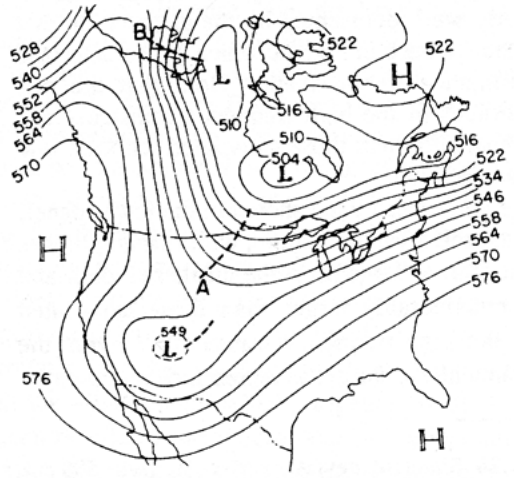

Fig. 19 500mb chart 00 GCT, 19 November, 1964.

2.4 Structure of the geopotential field

In the foregoing subsections we have described statistics derived directly from the horizontal wind field. As we proceed now to examine the structure of the transients in more detail, we will find it more convenient to deal with statistics based upon the geopotential height field. In extratropical latitudes, where the horizontal wind field tends to be quasi-nondivergent and its streamfunction closely resembles the geopotential height field, we will see a close relationship between the statistical properties of the wind field described in Section 2.2 and the structure of the geopotential height field as revealed by one point correlation maps described in this section.

Fig. 20 shows the distribution of temporal root mean square (rms) amplitude of the 500mb height field during the Northern winter in various frequency bands. The unfiltered data, shown in the upper panel, are dominated by three high latitude maxima: one over the North Atlantic, one over the North Pacific, and one over the northern European part of the Soviet Union. In all three centers the rms amplitudes are on the order of 180m.

The lowpass filtered data shown in the middle panel have been treated with a filter which removes disturbances with periods shorter than 10 days, which include baroclinic waves. The pattern is much the same, and the rms amplitudes are about 85% as large as their unfiltered counterparts. The variance that has been removed is fairly well represented by the distribution that was shown back in Fig. 4a, which is characterized by a much different shape. Note that the rms amplitudes of the high frequency transients are much smaller than those associated with the low frequencies.

30-day mean data, shown in the lower panel, also exhibit a similar pattern, with rms amplitudes about 50% as large as in the unfiltered data and still considerably larger than those associated with the high frequency transients. Even the interannual variability, as represented by 90-day

Fig. 20 Standard deviation of wintertime 500 mb height anomalies. *Top panel:* unfiltered, twice daily data. *Middle panel:* lowpass filtered data containing fluctuations with periods longer than 10 days. *Lower panel:* 30 day mean data. In units of meters; contour interval 10m. After Blackmon et al. (1984a).

means (not shown here), exhibits somewhat larger rms amplitudes than the high frequency variability that we associate with baroclinic waves.

A great deal of information concerning the transient variability of the geopotential height field is contained in the temporal covariance matrix

$$\mathfrak{R} \equiv \overline{Z_i' Z_j'}$$

where Z is the geopotential height at a particular level (such as 500 mb) and i and j are indices attached to particular gridpoints. The covariance between the ith and jth gridpoint is an element in this N x N matrix, where N is the number of gridpoints. The variance maps in Fig. 20 represent the diagonal elements in this matrix.

In order to expore more fully the structure in this matrix it is useful to view selected rows or columns, which represent the covariance between the variable in question (e.g., 500mb height) at a selected gridpoint and the same variable at all other gridpoints. It is convenient to normalize this field by dividing each element in $\mathfrak{R}$ by $\sigma_i \sigma_j$, where σ refers to the temporal standard deviation. The product $\sigma_i \sigma_j$ is given by the square root of the diagonal elements in row i and column j, respectively. The normalized matrix is called the *correlation matrix*, whose diagonal elements are all equal to unity, and whose off-diagonal elements are the correlation coefficients r_{ij}. Rows (or columns) in the correlation matrix are referred to as *one point correlation maps*. It is assumed that unless otherwise specified, correlation, in this context, refers to spatial autocorrelation [i.e., the temporal correlation between time series of the same variable at two different locations].

For any given *base gridpoint*, one point autocorrelation maps can be constructed for the fluctuations in any desired frequency band. This concept can also readily be extended to two different variables (i.e., cross correlation) and to the same variable at different lag times. They are analogous to the "structure functions" used in multivariate objective analysis.

Fig. 21 shows a selection of one point correlation maps for the gridpoint 55°N, 20°W, just to the west of the British Isles, which is the one emphasized by Sawyer (1970) in his pioneering study of low frequency variability. In all four panels of Fig. 21 the correlation is identically equal to one at the gridpoint, because the 500 mb height time series at the base gridpoint is perfectly correlated with itself. Since the characteristic horizontal scale of the geopotential height fluctuations is large in comparison to the distance between neighboring gridpoints, it follows that 500 mb height fluctuations at the base gridpoint exhibit a strong positive correlation with those at neighboring gridpoints: hence the region of positive correlations surrounding the base gridpoint in all four panels.

In the unfiltered data, the correlation contours surrounding the base gridpoint are circular. Hence, the correlation between 500mb height fluctuations at a given gridpoint and those at this particular base gridpoint appears to be uniquely determined by the distance between the selected gridpoint and the base gridpoint: i.e., it does not depend strongly upon the direction in which one travels to get from the base gridpoint to the selected gridpoint. Since the 500mb height fluctuations are not elongated in any particular direction, their horizontal gradients should not have any favored orientation, from which it follows that the corresponding geostrophic wind fluctuations should be nearly isotropic.

Another property of isotropic turbulence is a monotonic decay of the spatial autocorrelation function toward zero with increasing distance from the base gridpoint, and a complete absence of negative correlations. Beyond some "decorrelation" distance from the base gridpoint representative of the characteristic scale of the perturbations, the correlations should not be significantly different from zero. Hence, a one-point correlation map for isotropic turbulence should be characterized by a circular "bull's eye" pattern, centered on the base gridpoint and little else. Upon close inspection, it is evident that the correlation pattern for the unfiltered data in Fig. 21 does not quite meet this criterion. The most important discrepancy is the band of negative correlations to the south of the base gridpoint with the –0.41 center which, together with the concentric circles surrounding the base gridpoint, forms a meridionally oriented *dipole* or *seesaw* pattern over the eastern Atlantic. Evidently, when 500mb heights are above normal to the west of the British Isles, they tend to be below normal to the west of North Africa and *vice versa*.

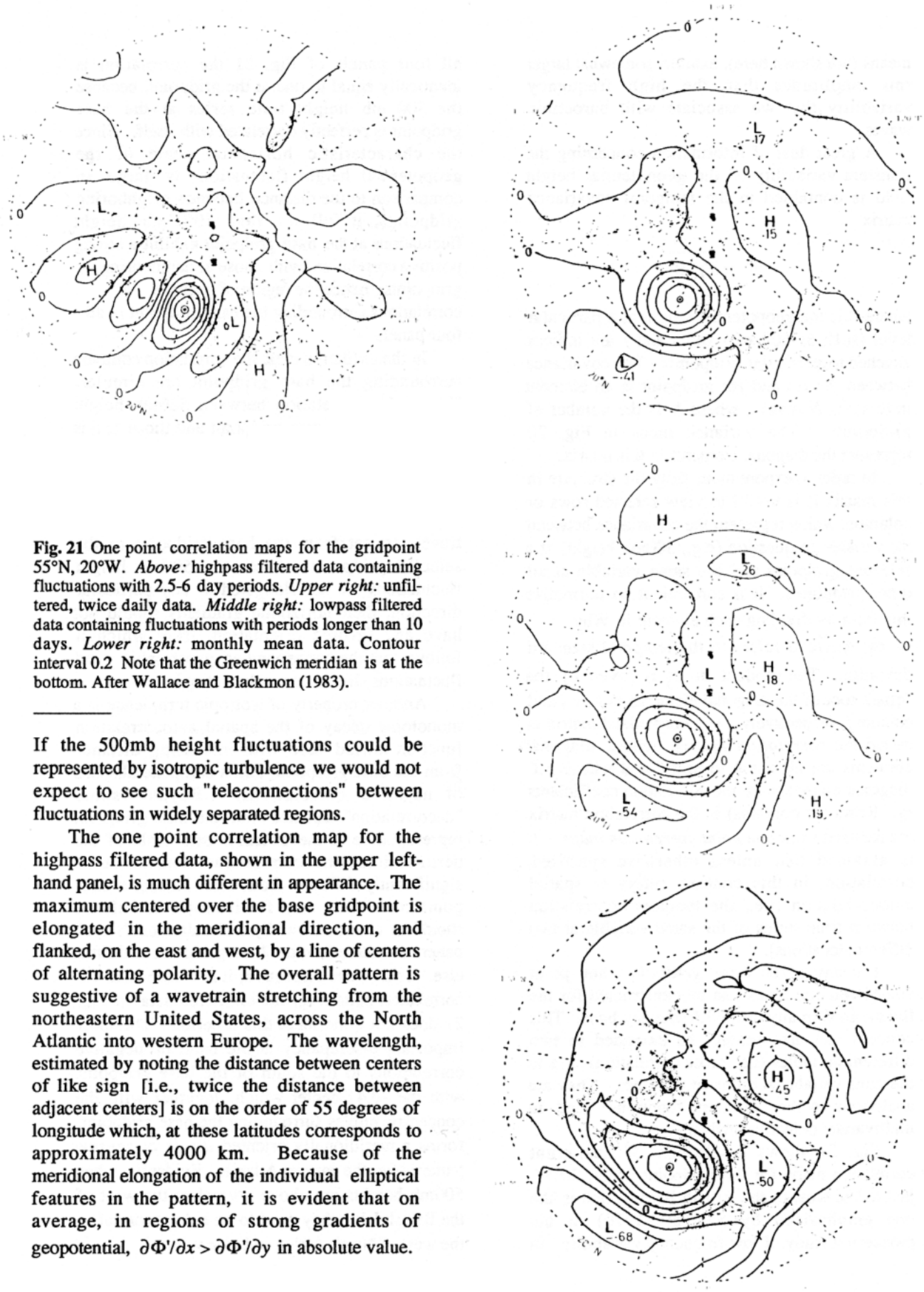

Fig. 21 One point correlation maps for the gridpoint 55°N, 20°W. *Above:* highpass filtered data containing fluctuations with 2.5-6 day periods. *Upper right:* unfiltered, twice daily data. *Middle right:* lowpass filtered data containing fluctuations with periods longer than 10 days. *Lower right:* monthly mean data. Contour interval 0.2 Note that the Greenwich meridian is at the bottom. After Wallace and Blackmon (1983).

If the 500mb height fluctuations could be represented by isotropic turbulence we would not expect to see such "teleconnections" between fluctuations in widely separated regions.

The one point correlation map for the highpass filtered data, shown in the upper left-hand panel, is much different in appearance. The maximum centered over the base gridpoint is elongated in the meridional direction, and flanked, on the east and west, by a line of centers of alternating polarity. The overall pattern is suggestive of a wavetrain stretching from the northeastern United States, across the North Atlantic into western Europe. The wavelength, estimated by noting the distance between centers of like sign [i.e., twice the distance between adjacent centers] is on the order of 55 degrees of longitude which, at these latitudes corresponds to approximately 4000 km. Because of the meridional elongation of the individual elliptical features in the pattern, it is evident that on average, in regions of strong gradients of geopotential, $\partial\Phi'/\partial x > \partial\Phi'/\partial y$ in absolute value.

Therefore, the meridional component of the geostrophic wind should tend to be stronger than the zonal component in the high frequency transients, in agreement with the results presented in Figs. 14, 15 and 17. Furthermore, the different shapes of the variance patterns for the zonal and meridional wind components in Fig. 14 (i.e., the peculiar dumbell shape for the zonal wind field in Fig. 14, with maxima along 35° and 50°N, as opposed to the simpler shape for the meridional wind field with the single maximum along 45°N is consistent with the wave pattern in Fig. 21: zonal geostrophic winds should be strongest on the northern and southern flanks of the stormtrack, where $\partial\Phi'/\partial y$ attains its largest absolute values; whereas the meridional geostrophic wind component should be strongest along the axis of the stormtrack, where $\partial\Phi'/\partial x$ is largest.

Upon close inspection, the features in this panel are not quite elliptical in shape: the major axes are curved slightly so that the ellipses are more convex on the eastern side than on the western side. The distortion is particularly evident in the eastern centers of the wavetrain. Equatorward of the base gridpoint, the wave axes associated with the high frequency transients exhibit a northeast-southwest tilt indicative of a poleward flux of westerly momentum; while poleward of the base gridpoint they exhibit a more subtle northwest-southeast tilt indicative of an equatorward flux of westerly momentum, consistent with results presented in Fig. 14c.

Not only are the patterns in Figure 21 consistent with variance and covariance statistics presented in Figs. 14, 15 and 17, but they also provide a kinematic interpretation of the anisotropy of the wind statistics in terms of the characteristic shape of the streamfunction associated with the high frequency transients.

The right-hand panels in Fig. 21 may be viewed as a sequence, starting with unfiltered data in the top panel, proceeding to lightly lowpass filtered data in the middle panel, and on to strongly lowpass filtered data in the lower panel. Note the gradual change in appearance of the correlation patterns as successively more of the higher frequency transients are removed by the filtering procedure. The concentric contours surrounding the base gridpoint become progressively more elongated in the east-west direction, the negative correlations to the west of North Africa become progressively stronger, and a planetary-scale wavetrain to the east of the base gridpoint, which is only hinted at in the unfiltered data, emerges in the correlation pattern. The pronounced zonal elongation of the features over the Atlantic sector in the monthly mean data (lower panel) is indicative of strong anisotropy in the winds, with much more kinetic energy in the zonal component than in the meridional component, consistent with results presented in Figs. 15 and 17.

Hence, the high and low frequency transients are characterized by distinctly different horizontal scales and orientations. The transients as a whole, as reflected in the unfiltered data, are more isotropic in appearance than the high and low frequency transients because there is evidently some cancellation between the high and low frequency contributions to the correlation matrix.

The relationship between the one-point correlation maps and the anisotropy of the horizontal wind field is further illustrated by Fig. 15, which shows the 0.3 contours surrounding the base gridpoint on selected one-point correlation maps, superimposed upon the minor axes of the ellipses associated with the velocity correlation tensor. With only a few minor exceptions, the line segments derived from the wind statistics are oriented parallel to the minor axes of the elliptical loops traced out by the correlation contours. Of particular interest in this figure is the sharp contrast between the structure of the high and low frequency transients over the oceanic sectors.

2.5 The dominant correlation patterns

Individual one point correlation maps such as the example shown in Fig. 21 provide some useful insight into the horizontal structure of the transients. However, it would be extremely tedious to inspect the hundreds of such maps that would be required to document in detail the structures inherent in the temporal correlation matrix $\mathcal{R} \equiv \overline{Z_i' Z_j'}$. We would like to find a more efficient way of characterizing the one-point correlation maps and identifying the most interesting ones. For example, are the distributions in Fig. 21 typical of the one-point correlation maps? If one had used a base gridpoint, say 30° longitude father to the east or south of the one used in Fig. 21, would the patterns have been similar in appearance, but merely shifted in longitude or latitude by an

amount comparable to the shift in the base gridpoint? The suspicious reader might wonder whether they might perhaps be less convincing than those shown in this hand-picked example.

One simple way of characterizing the patterns in the one-point correlation maps is (1) to note the absolute magnitude of the strongest negative correlation appearing anywhere in the map, (2) to assign that correlation to *the base gridpoint* (not to the point with which it exhibited the strong negative correlation), and (3) to prepare a single map displaying these correlations. Formally, this procedure is identical to (1) selecting the strongest negative value in each row or column of the correlation matrix and dropping the minus sign, (2) defining a new column matrix, $\boldsymbol{T}$, whose elements T_j are these strongest negative correlations. Following Wallace and Gutzler (1981), we will refer to $\boldsymbol{T}$ as the distribution of *teleconnectivity*.

Figure 22 shows the distribution of teleconnectivity for the wintertime 500mb height field in three different frequency bands. The high frequency transients with periods shorter than 6 days, shown in the upper panel, are characterized by elongated bands of relatively high teleconnectivity along 40°N, centered over the western oceans, and a weaker maximum over the Mediterranean. The base gridpoint in Fig. 21 is located just to the east of one of these maxima. The arrows in this panel are drawn from each gridpoint toward the gridpoint with which it exhibits the strongest negative correlation.

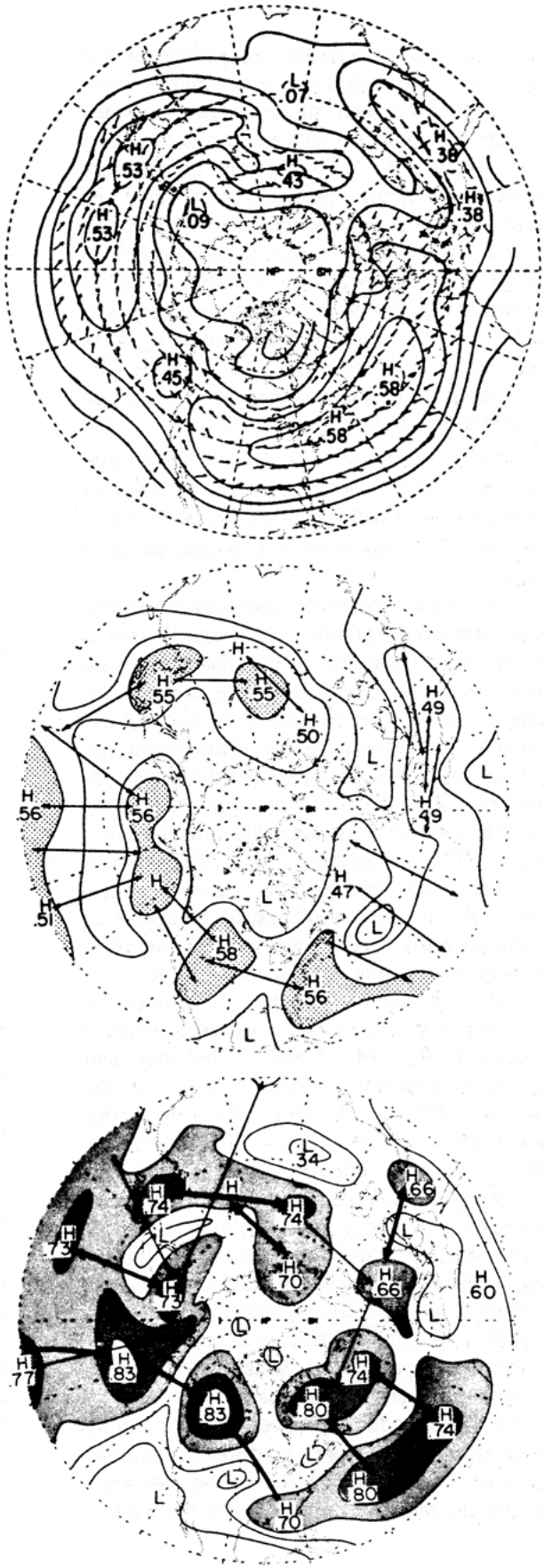

Fig. 22 The hemispheric distribution of teleconnectivity for wintertime 500mb height. *(Upper panel):* as constructed from highpass filtered data containing fluctuations with periods shorter than 6 days. Contour interval 0.05. Arrows are drawn from each gridpoint in the direction of the gridpoint with which its highpass filtered 500 mb height time series exhibits the strongest negative correlation and halfway to that gridpoint. After Wallace et al. (1988). *(Middle panel):* as constructed from bandpass filtered data containing fluctuations with periods between 10 and 30 days. *(Lower panel):* based on 30–day means. In the lower two panels, the contour interval is 0.1 and arrows are drawn from selected gridpoints all the way to the gridpoints with which their filtered 500 mb height timeseries exhibit the strongest negative correlation. Lower two panels after Blackmon et al. (1984a).

In order to avoid overlapping of the lines, their length is only half the distance to that gridpoint. Note that the arrows have an east-west orientation, and if their length is doubled it becomes comparable to the distance between the base gridpoint and the strongest negative centers in the high frequency panel of Fig. 21. Hence, the east-west oriented "wavetrain" structure evident in Fig. 21 is representative of one-point correlation maps throughout much of middle latitudes. Over the western oceans the wavetrain patterns should be even stronger than the sample shown in Fig. 21, while over Eurasia they should be less prominent. Over polar regions, where the teleconnectivity is much lower, the patterns on the one-point correlation maps should be more like the isolated circular "bull's–eyes" that we associate with isotropic turbulence.

The corresponding teleconnectivity pattern based on monthly mean data, shown in the lower panel, exhibits an equally distinctive, but entirely different pattern, with maximum values in excess of 0.8, separated by regions of lower teleconnectivity. Hence, some one-point correlation maps for the monthly mean data exhibit much stronger patterns than others.

The base gridpoint that was used in generating the sample in Fig. 21 is located close to the 0.74 maximum in the eastern Atlantic. The arrow in Fig. 22 connects it with the gridpoint with which it exhibits the -0.74 correlation on its one-point correlation map. Consistent with Fig. 21, this point is located to the west of North Africa. Note that teleconnectivity is a reciprocal property: the one point correlation map for the base gridpoint to the west of North Africa contains a -0.74 negative center to the west of the British Isles. But for a sign reversal, the one-point correlation maps for base gridpoints in these two regions exhibit similar features. Base gridpoints halfway between (i.e., around 40°N) do not exhibit as strong negative "centers of action" [i.e., regions in which 500 mb height is negatively correlated with the timeseries at the base gridpoint]. Note that the secondary centers over Europe and Asia in Fig. 21 (lower panel) also appear as local teleconnectivity maxima in Fig. 22 (lower panel). Hence, on a single map, we are able to portray many of the more prominent features that appear on individual one-point correlation maps.

Fig. 22 (lower panel) contains several centers with teleconnectivities as strong as those just mentioned. There is evidence of dipole structures over the western Atlantic and Pacific and a more complex pattern with four interconnected centers extending along an arc from the Hawaiian Islands to the southeastern United States. Let us explore these features in more detail.

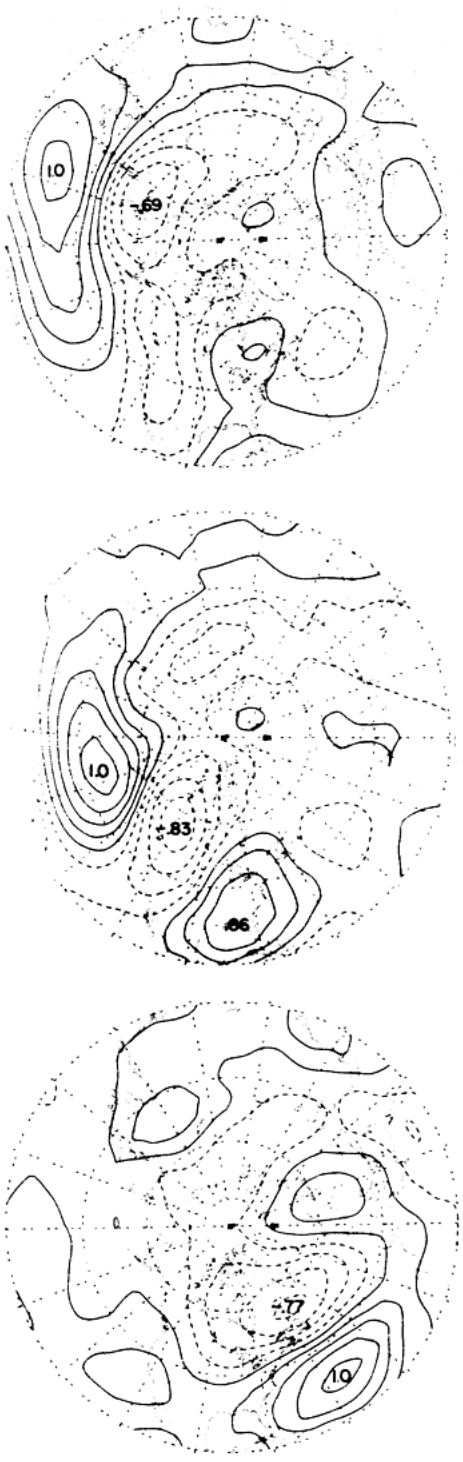

Fig. 23 One point correlation maps for the base gridpoints 30°N, 155°E; 45°N, 165°W, and 30°N, 55°W, which are centers of action in the WP, PNA and WA patterns, respectively. Contour interval 0.2; negative contours are dashed. Based on wintertime, 30-day mean 500mb height data. After Blackmon et al. (1984).

Fig. 23 shows a selection of representative one-point correlation maps associated with some of the more prominent patterns in the teleconnectivity field shown in the previous figure. From top to bottom, we will subsequently refer to them as the Western Pacific (WP), Pacific/North American (PNA) and Western Atlantic (WA) patterns, respectively. We will refer to the pattern in the lower panel of Fig. 21 as the Eastern Atlantic (EA) pattern. Further documentation of these patterns is given in Wallace and Gutzler (1981) and Esbensen (1984). The fact that the same four patterns emerge among the leading rotated principal components[11] of the wintertime low-frequency 500mb height field [e.g., see Horel (1981), Barnston and Livezey (1987)] attests to their statistical and dynamical significance. Furthermore, Dole and Gordon (1983) and Dole (1983, 1986a,b) identified structures remarkably similar to the PNA and EA patterns in their studies of persistent anomalies in the wintertime circulation, which was based on an entirely different analysis technique.

---

11 Rotated principal components are linear combinations of a subset of the temporal coefficients (i.e., the *principal components*) associated with conventional empirical orthogonal functions or eigenvectors of the temporal covariance matrix $\mathfrak{R}$. The purpose of the rotation is to simplify the associated spatial patterns and render them more robust. The rotated principal components are not as efficient at explaining the variance of the observed fields as the conventional ones, but they tend to be much more meteorological in appearance and they are often much more robust [e.g., see the demonstration in Hsu and Wallace (1985)]. The principal components retain their orthogonality during the rotation but the associated spatial patterns are not constrained to remain orthogonal. The method is not completely objective, because the number of principal components to be rotated must be specified, However, for reasonable choices of the number to be rotated, the results do not appear to be particularly sensitive to this choice. In general, the more principal components that are rotated, the simpler the resulting spatial patterns, and the more the leading patterns resemble an interesting selection of one-point correlation maps. This method is capable of identifying significant monopole patterns which would not be apparent in an analysis based upon teleconnectivity. For an extensive discussion and comparison of observational results based on this method, the reader is referred to Barnston and Livezey (1987).

As demonstrated in Fig. 24, qualitatively similar patterns are evident in one point correlation maps based on lightly lowpass filtered [e.g., 5-day mean] data, monthly mean data and wintertime [90-day] mean data. Hence, the gross features of the structure of low-frequency variability do not appear to be overly sensitive to the high-frequency cutoff provided that fluctuations with periods shorter than 10 days are excluded. We have learned that this apparent insensitivity is due, in part, to the redness of the frequency spectrum of atmospheric variability, which was commented upon at the beginning of Section 4. For example, the interannual variability of wintertime mean 500 mb height, whose structure is reflected in the bottom panel of Fig. 24, accounts for about half the month-to-month variability, whose structure is reflected in the middle panel, and about 25% of the variance of 5-day means, whose structure is reflected in the top panel. In other words, there is a considerable amount of redundancy built into the patterns in Fig. 24.

We can eliminate this redundancy by examining the structure of the low-frequency variability in mutually exclusive frequency subranges. For this purpose it is instructive to contrast the structure of what we will subsequently refer to as the *very low frequency variability* inherent in monthly mean data, with the structure of what we will refer to as *intermediate frequency variability*, with periods in the 10–30 day range, as isolated with a bandpass filter. The results shown here are extracted from a more extensive analysis presented in Blackmon et al. (1984a).

Fig. 24 One-point correlation maps for the base gridpoint (45°N, 165°W) based on wintertime 500mb height data. Upper panel: lowpass filtered data containing fluctuations with periods longer than 10 days. Middle panel: 30-day mean data, overlapping at 10-day intervals. Lower panel: 90-day mean data. After Blackmon et al. (1984a).

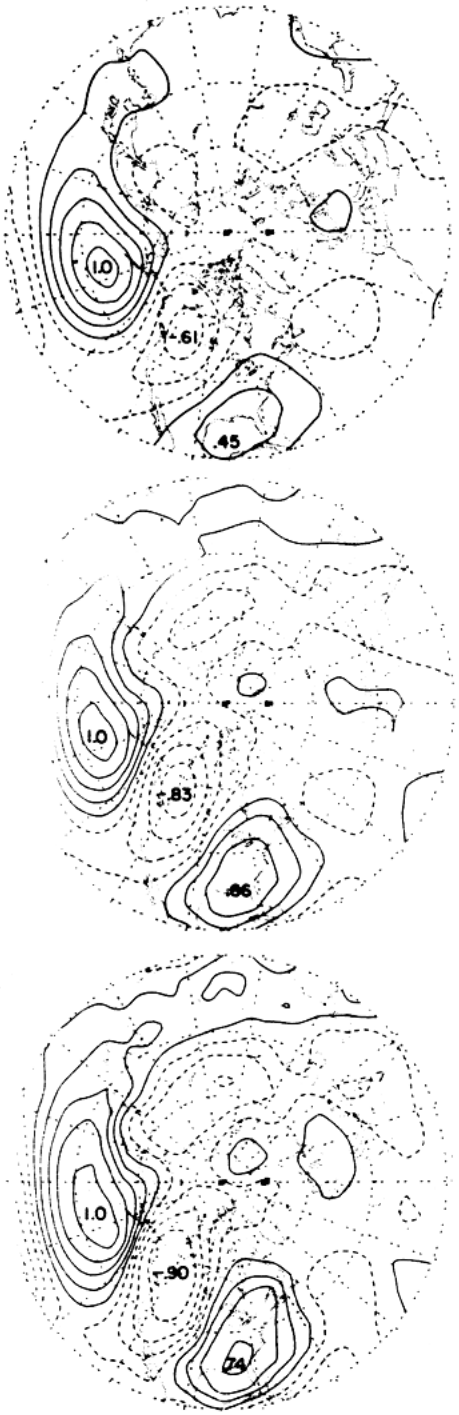

Figure 25 shows three successive samples from the set of one-point correlation maps for base gridpoints lying along the 30°N latitude circle, from left to right: 85°W, 70°W and 55°W. The upper panels are based on 30-day mean data which resolves only very low frequency fluctuations periods longer than 60 days, while the lower panels are based on bandpass filtered data, in which intermediate frequency fluctuations with periods from 10-30 days are emphasized.

Scanning the upper panels from left to right, one sees an interesting evolution as the base gridpoint shifts eastward along the 30° latitude circle. The PNA pattern is prominent in the left-hand panel, and the WA pattern dominates the right-hand panel. The middle panel contains elements of both patterns, but the correlations are not as strong as in the left and right-hand panels. The evolution of the patterns is somewhat analogous to the sequence of sounds that one hears when one tunes a radio dial. The PNA "station" comes in clearly in the left-hand panel, but it fades out as the base gridpoint is shifted eastward. At the middle gridpoint there is interference between the PNA and WA "stations" and neither one comes in clearly. By the time the "dial" has been turned to the location of the right-hand gridpoint, the WA "station" is coming in loud and clear and PNA is no longer audible. This sequence is suggestive of geographically fixed structures resembling "normal modes".

The corresponding sequence for the lower panels is somewhat different. The pattern in the left-hand panel resembles the PNA pattern in some respects, but the negative center over western North America is farther to the south than in the PNA pattern and the characteristic north-south dipole pattern in the Pacific is virtually absent. The overall pattern resembles an east-west oriented wavetrain not unlike those observed at the high frequencies, but with longer zonal wavelength. The patterns in the middle and right-hand panels are qualitatively similar, but the centers in each panel are shifted eastward by about 15° of longitude relative to those in the previous panel [i.e., by an amount comparable to the shift in the location of the base gridpoint. It is as if the whole pattern were lifted up and shifted bodily with the base gridpoint. Hence, the very low frequency teleconnection patterns appear to be geographically fixed, while the intermediate frequency patterns tend to retain a more or less fixed shape relative to the base gridpoint. Furthermore, the patterns in the two frequency ranges exhibit contrasting types of anisotropy; the former being elongated in the east-west direction and the latter in the north-south direction.

The contrasting structures of the very low frequency and intermediate frequency variability are also evident in the teleconnectivity maps shown in Fig. 22. In comparison to the teleconnectivity based upon monthly mean data (lower panel), the teleconnectivity distribution of the 10-30 day period fluctuations (middle panel) is much more uniform, with values ranging from 0.40-0.55 over most of the hemisphere. The north-south oriented dipole structures over the oceanic sectors are not as strong as they are in the lower frequency variability and the pattern is dominated by three west-northwest— to east-southeast oriented wavetrains: one extending from the North Pacific, across the United States, and into the subtropical North Atlantic; one extending from Spain, across the Mediterranean and Middle east, into the Persian Gulf, and one extending from central Siberia, across Japan, and into the subtropical western Pacific. The features in the lower panels of Fig. 25 are manifestations of the first of these wavetrains.[12]

We will contrast the structure of the very low and intermediate frequency variability further in Section 2.12, after we have discussed the time evolution of the fluctuations in various frequency bands.

---

[12] Y. Kushnir has recently shown that these wavetrains show up as pairs of rotated principal components of the covariance matrix for the 10-60 day period fluctuations, as isolated by time filtering. They are not present at lower frequencies. The WA, WP and EA patterns shown in Figs. 21 and 23 figure most prominently in the lower frequency, intraseasonal variability with periods between 60 and 180 days, whereas the PNA pattern and the North Atlantic Oscillation (see Section 2.12) are most prominent in the interannual variability.

Fig. 25 *Upper panels:* One point correlation maps for the base gridpoints (30°N, 85°W), (30°N, 70°W), and (30°N, 55°W), *left to right*, based on 30-day means, overlapping at 10-day intervals, for wintertime 500mb height data. *Lower panels*: as in upper panels, but for bandpass filtered data containing fluctuations with periods between 10 and 30 days. After Blackmon et al. (1984a).

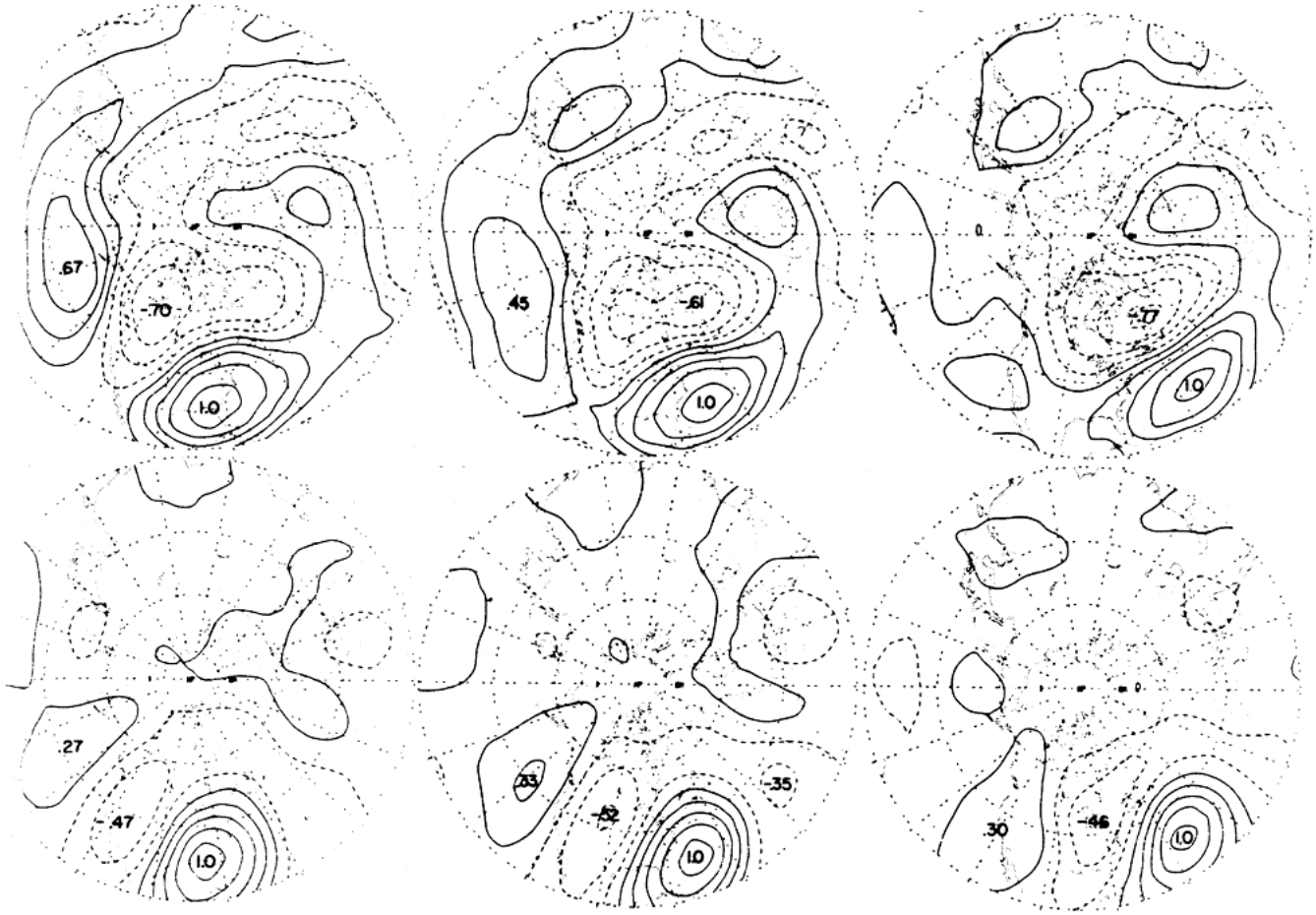

Fig. 26 Timeseries of an index of the PNA pattern. The solid curve represents data that have not been subjected to any filtering whatsoever in the time domain and the dashed curve represents data that have been lightly lowpass filtered to remove fluctuations with periods shorter than 10 days. Courtesy of H. Nakamura.

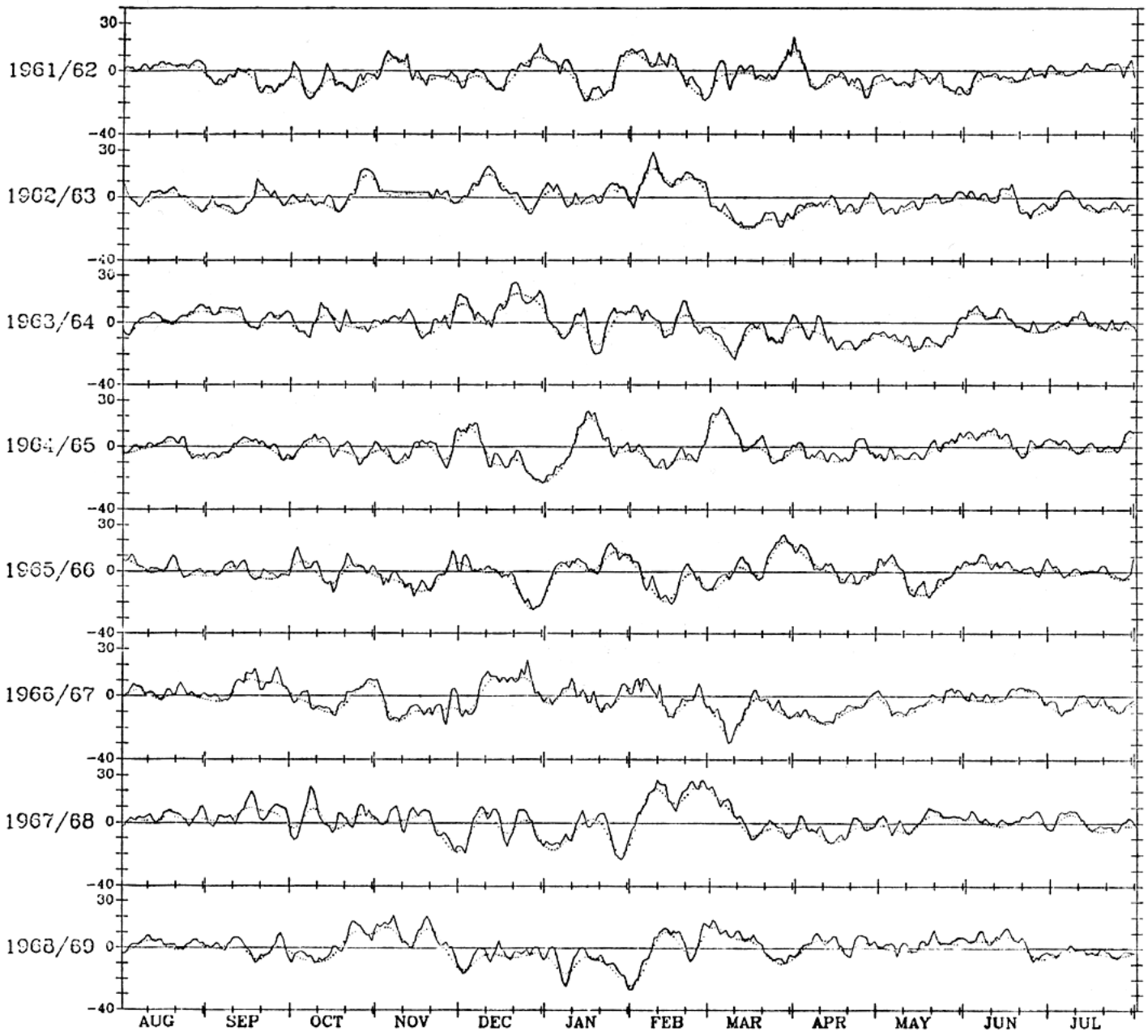

2.6 Time evolution

Fig. 26 shows extended timeseries of an index of the PNA pattern, based upon daily data. The index is constucted by projecting the anomalies in the daily data upon the PNA anomaly pattern, using the following procedures:

(1) The four-point index defined by Wallace and Gutzler (1981); i.e.,

$$R = [Z^*(20°N, 160°W) - Z^*(45°N, 165°W) + Z^*(55°N, 115°W) - Z^*(30°N, 85°W)]/4$$

where Z^*, the normalized 500mb height anomaly is correlated with 500 mb height at every gridpoint to generate a correlation pattern analogous to a one-point correlation map. The resulting map mat be viewed as the average of the one-point correlation maps for the four "centers of action" of the PNA pattern.

(2) Correlations in excess of 0.3 on this hybrid correlation map are used as weighting factors w_j which are subsequently multiplied by the daily values of normalized 500 mb height anomalies at each respective gridpoint j to generate the timeseries

$$PNA(t) = \Sigma w_j Z_j(t) / \Sigma w_j$$

whose daily values are plotted in Fig. 26.

It is notable that even the unfiltered time series in Fig. 26 is dominated by the low frequencies. The projection of the daily data upon the PNA pattern has, in effect, filtered out much of the high frequency variability in the gridpoint data. Had the same daily data been projected upon a spatial correlation pattern characteristic of baroclinic waves, the resulting timeseries would have had a much differerent character.

The low frequency variability inherent in the PNA timeseries is rather complicated. In some winters the timeseries exhibits a sinusoidal behavior, while in others it remains in one polarity for extended periods and exhibits what some might be tempted to regard as abrupt "phase transitions" between different "climatic states". The extent to which randomly generated "red noise" timeseries would exhibit similar types of behavior has not been completely determined. Dole (1986b) did not find evidence of bimodality in the timeseries of the pattern indices themselves, but Sutera and collaborators have shown that an index of the energy of the low-frequency planetary waves does exhibit a multimodal frequncy distribution[13]. Analogous indices for the other patterns (not shown) exhibit characteristics qualitatively similar to the example shown in Fig. 26.

The two-dimensional correlation matrix $\Re$, which was discussed extensively in the previous section, may be viewed as a slice out of the three-dimensional lag-correlation matrix, whose elements are $Z_i'(t)\ Z_j'(t+\tau)$, where i and j are the gridpoint identifiers and τ is the lag interval, which may be either positive or negative.

As the absolute values of τ becomes large in comparison to the predominant timescales inherent in the atmospheric data, the lag correlations must approach zero. Hence, only a finite range of values of τ will be of interest. Specifically, we are interested in that range of values in which τ is large enough to allow some significant change in the shape, orientation, or position of the correlation patterns, relative to the simultaneous correlations discussed in the previous section, but small enough to retain statistical significance of the patterns.

There is no guarantee that such a range of values will exist. For example, suppose that we take random, unrelated, "red noise" time series of a number of indices such as *PNA*, and multiplied them by their respective spatial pattern vectors to generate an array of synthetic gridpoint data. If this synthetic data set were subjected to lag correlation analysis, the simultaneous correlation patterns would appear without change in shape, orientation or position in the lag-correlation maps, and these patterns would simply fade into obscurity as the lag interval was increased.

Figure 27 shows lag correlation maps at one day intervals for the high frequency fluctuations. The simultaneous correlation map appears in the middle panel and in the upper maps the timeseries at the base gridpoint is correlated with the hemispheric array of gridpoints one day earlier, two days earlier, etc, proceeding upward in the sequence. Hence, we may view this sequence of maps as portraying the high frequency fluctuations on Day –3, Day –2,.....Day +3, where Day 0 is the time at which the primary positive center in the anomaly pattern is located precisely over the base gridpoint.

It is evident that the positive center located over the base gridpoint on Day 0 is located about 10 degrees of longitude farther to the west on

[13] Alfonso Sutera will be describing these results in his lecture.

Day–1 , 20 degrees of longitude farther to the west on Day –2, etc. Viewing the entire sequence, it is apparent that this feature takes a track southeastward from central Siberia, across Korea, and then more or less due eastward along the 40° latitude circle with a phase speed of about ten degrees of longitude per day, which corresponds to about 10 m s^{-1}. By viewing the sequence of maps at the base gridpoint or other fixed gridpoints in the vicinity, it is readily apparent that the corresponding period of these waves as they propagate eastward past a fixed gridpoint is on the order of 4–5 days. The correlation pattern fades out as the lag interval increases , but a statistically significant pattern is present out to five days in either direction. The "kidney bean " shape of the wave pattern is particularly evident at the positive lags (i.e., in the lower panels).

The local phase speed and direction of these waves can be estimated quite accurately by tracking the primary positive center in the lag-correlation maps from its position on Day –1 to its position on Day +1, and dividing this displacement by the two-day interval to obtain a vectorial "phase velocity"[14]. This process can be automated in a computer program. Figure 28 shows a selection of these vectors, based upon wintertime 500 mb height data (indicated by the solid arrows), superimposed upon the climatological mean wintertime 700 mb geopotential height field (indicated by the contours). A few climatological mean 700 mb geostrophic wind

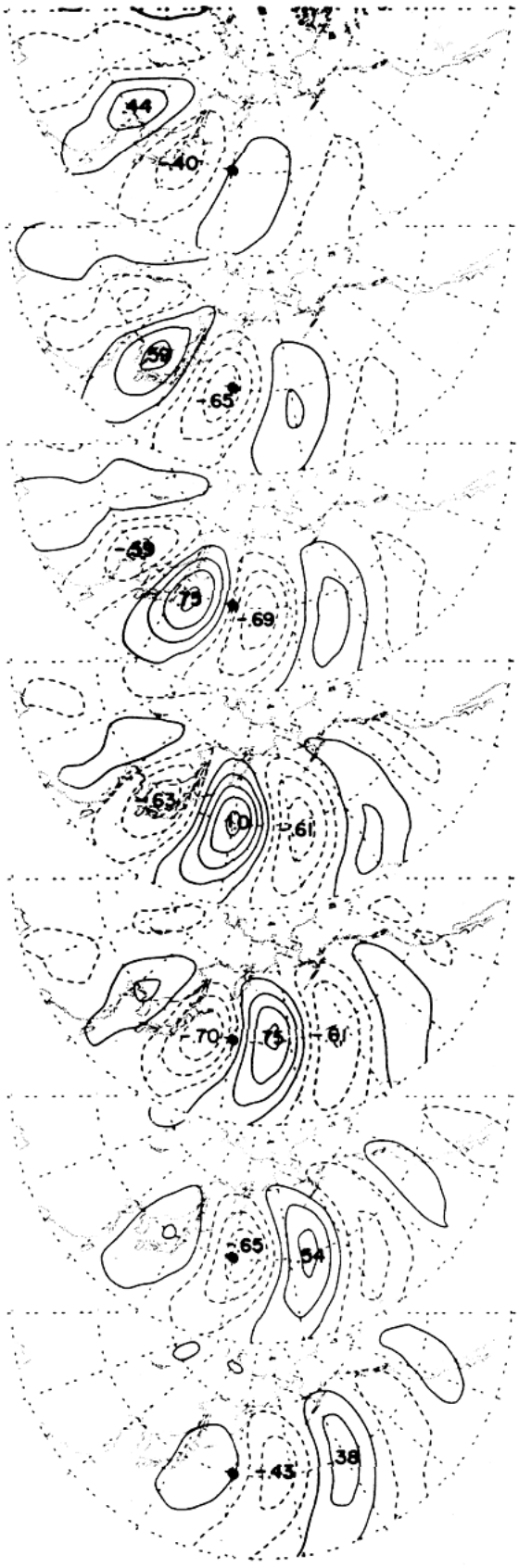

Fig. 27 Lag-correlation maps between high frequency (2.5-6-day period) fluctuations in wintertime 500 mb height at the base gridpoint (40°N, 160°E) and 500mb height over the Pacific sector at one day intervals. Middle panel: simultaneous correlation map. Upper panels: 500 mb height at other gridpoints leading that at the base gridpoint. Lower panels: 500 mb height at other gridpoints lagging that at the base gridpoint. Contour interval 0.2 (contours for -0.1, 0.1, 0.3, etc.) After Blackmon et al. 1984b.

[14] Strictly, speaking, the phase propagation, c is not a vectorial field, since $c_x^2 + c_y^2 \neq c^2$.

vectors, derived from the height field are also indicated as dashed arrows, for purposes of comparison. It is evident that to a rather good approximation, the mean 700mb wind field serves as a "steering flow" for the phase velocity vectors. This result is consistent with an interpretation of the high frequency transients in terms of baroclinic waves; since the latter have a steering level near 700 mb [e.g., see Holton, (1979)].

Flg.. 28 Solid arrows are "phase velocity" vectors for high-frequency (2.5-6-day period) wintertime 500 mb height fluctuations derived from lag-correlation statistics as explained in the text. Contours represent the climatological mean wintertime 700 mb height field and the dashed arrows represent a selection of 700 mb geostrophic wind vectors derived from the geopotential height field.

A distinctly different form of time evolution is observed at the lower frequencies, as illustrated by the lag-correlation maps for lowpass filtered data shown in Fig. 29. These maps contain fluctuations with periods on the order of 10-days or longer. The left-hand panels represent conditions three days previous to the"reference timeseries" at the base gridpoint, and the right-hand panels represent conditions three days later. Hence, by comparing left and right-hand panels in Fig. 29, one obtains an indication of the evolution of the low-frequency patterns over the course of a six day time interval.

The three selected examples shown in Fig. 29 differ with respect to certain interesting details which we will comment on presently, but they share a number of features which appear to be characteristic of low-frequency fluctuations in general. They usually exhibit some eastward phase propagation, but considering the 6-day interval between the left and right-hand panels in the Figure, the phase velocities are much smaller than those associated with the high frequency fluctuations. Simple phase propagation is clearly not the dominant form of time evolution at the low frequencies. In all three panels, we see evidence of the weakening or disappearance of upstream (western) features of the pattern from Day –3 to Day +3, and the appearance or strengthening of downstream features. This behavior is most striking in the top panels, in which we see (1) the upstream, negative center over northern Europe disappear, (2) the downstream center near Korea strengthen (from -0.33 to -0.55), and (3) a new positive center form still farther downstream over the subtropical western Pacific during the 6-day interval from Day –3 to Day +3. Note that during this interval, the primary positive center near the base gridpoint hardly moves at all.

The base gridpoint used in generating the maps in the middle panel may be recognized as one of the "centers of action of the PNA pattern. The evolution of this pattern is a bit more subtle, but one can see the shift in emphasis from the upstream centers over the North Pacific toward the downstream centers over North America. A similar evolution is observed for the EA pattern (not shown).

The lower panels exhibit a somewhat more complex evolution. In the left-hand panel a wavetrain appears to be dispersing across the United States toward the subtropical North Atlantic. In the right-hand panel the North American wavetrain has disappeared and there is a hint of a wavetrain emanating from the subtropical North Atlantic and dispersing northeastward toward Scandinavia. It is almost as if the original underwent some kind of reflection from the subtropical Atlantic.

Fig. 29 Selected pairs of lag-correlation maps for wintertime, low-frequency (>10-day period) 500-mb height fluctuations. *Left-hand panels:* three days earlier than the fluctuations at the base gridpoint. *Right-hand panels:* three days later than the fluctuations at the base gridpoint. *Top panels:* for the base gridpoint (55°N, 75°E). *Middle panels:* for the base gridpoint (55°N, 115°W). *Lower panels:* for the base gridpoint (30°N, 85°W). After Blackmon et al., 1984b.

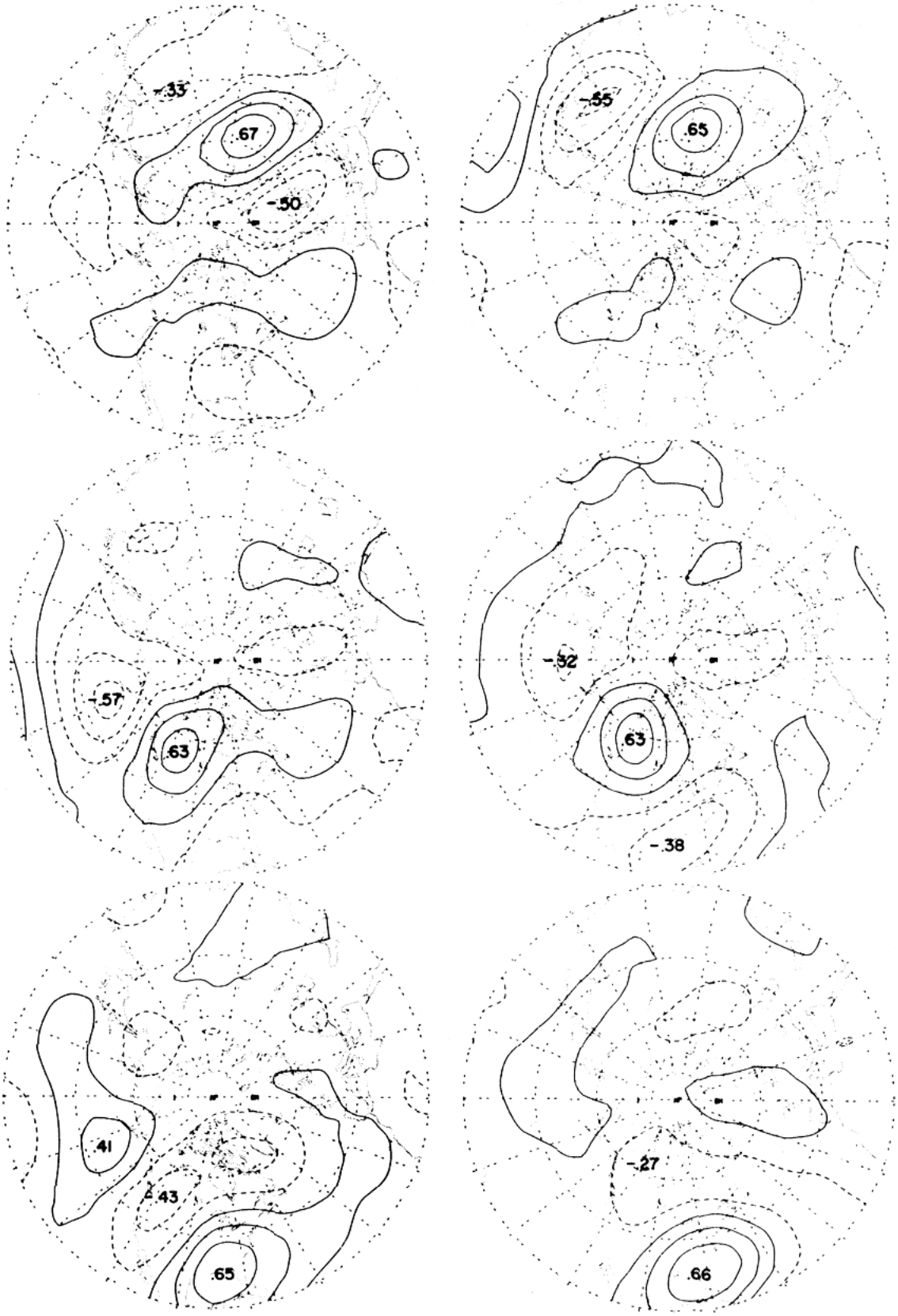

The sequences in Fig. 29 are suggestive of energy dispersion through wavetrains whose phase velocity relative to the ground is negligibly small. The rate at which upstream centers disappear to be replaced by new downstream centers gives an indication of the group velocity associated with this process. It is evident from this figure that the group velocity relative to the ground is in the general direction of the upper air climatological mean flow.

A similar type of behavior is observed in the barotropic model, as illustrated in the sequence of streamfunction patterns shown in Figs. 30 and 31. In these integrations one can see the development of wavetrains downstream of a vorticity source. In the case of the tropical source, the wavetrain exhibits strong meridional propagation into middle latitudes. Successive new centers develop and intensify along the leading edge of the wave packet, while the established centers closer to the vorticity source remain geographically fixed. Eventually the packet disperses all the way around the globe and returns to the source region, weakened by the damping that it has been subject to along the way. The group velocity of the waves is related to the rate at which the wavetrain forms and disperses eddy kinetic energy around the globe.

Now let us imagine a complementary set of numerical experiments in which the wavetrain is fully established in the initial conditions and the vorticity source is turned off on Day-Zero. Since the model is linear, it is clear that the decay of the wavetrain must begin at the former vorticity source and manifest itself in the decay of successive downstream centers of the wavetrain as that same group velocity vector reaches them, carrying with it the information that the vorticity source has been turned off.

Now, let us imagine that the vorticity source is turned on on Day-Zero and turned off a few days later. The linear response can be inferred by superimposing the development and decay sequences described above. The result would be a wave packet, emanating from the source, with new centers developing downstream (in terms of the group velocity) while older centers on the upstream end of the wave packet decay.

Energy dispersion in the real atmosphere is, of course, much more complicated, with nonlinear effects, baroclinic processes, a much more complicated background flow, etc. This simple illustration is merely intended to show that a process as fundamental as low-frequency, linear Rossby-wave dispersion from a fixed source exhibits a time evolution qualitatively similar to that observed for low-frequency geopotential height fluctuations in the atmospheric circulation.

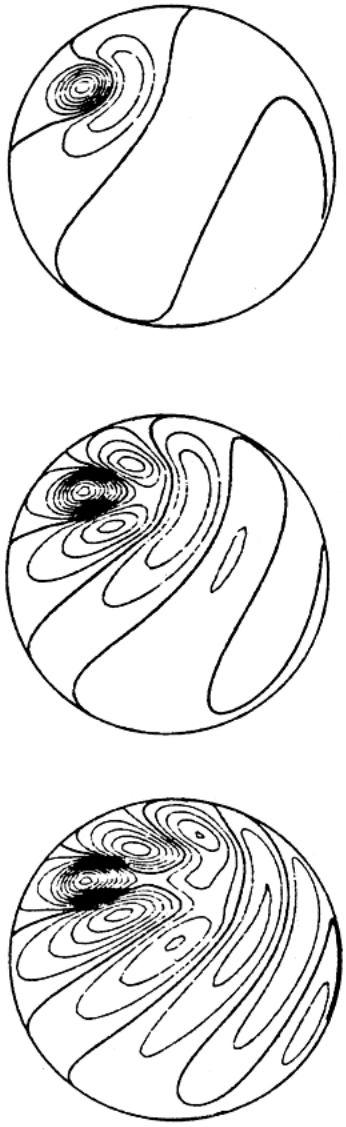

Fig. 30 Streamfunction maps on Day-2 (upper), 5 (middle), and 8 (lower) of a numerical integration with a linear barotropic model with a steady-state vorticity source, inserted at Day-Zero into the a background flow consisting of pure superrotation. After Hoskins (1983).

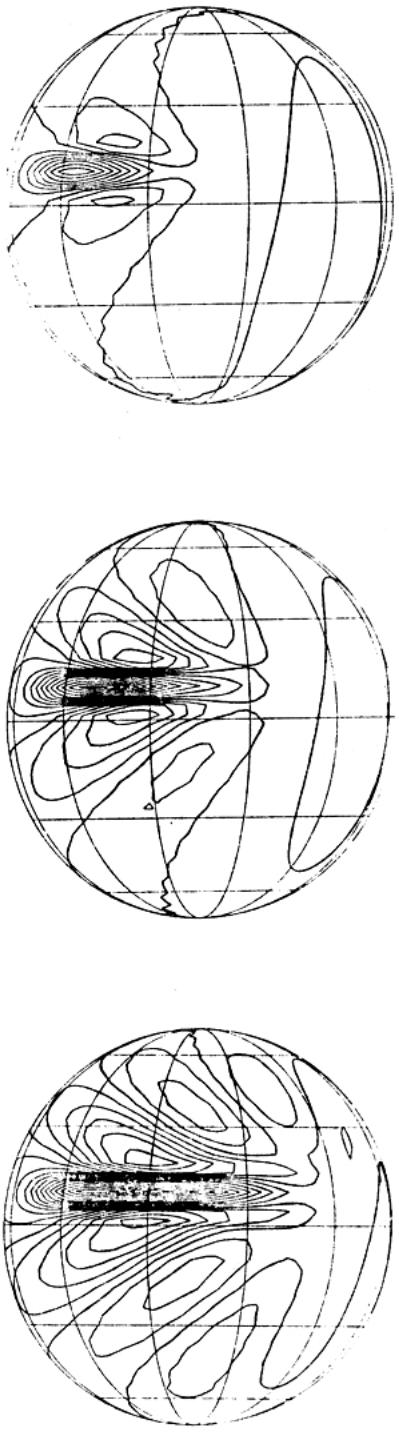

Fig. 31 As in Fig. 30 but for a vorticity source located at 15°N. Courtesy of B.J. Hoskins.

Pairs of lag-correlation maps analogous to those in Fig. 29 can be generated for data that have been more strongly lowpass filtered: for example, we could consider –1 and +1 month lag correlation maps based upon monthly mean data. Blackmon et al. (1984b) have shown that the evolution that one observes in such sequences is less interesting than that observed in more lightly lowpass filtered data. In general, as the lowpass filter is made stronger and the lag interval is increased accordingly, the patterns in the lag correlation maps become muted versions of their counterparts on the simultaneous correlation maps.

Experienced synopticians have been aware of the downstream development of new ridges and troughs in quasi-stationary wavetrains since the advent of upper air maps during the 1940's. They have also noticed a tendency for low-frequency features to propagate westward against the mean flow — a phenomenon often referred to as retrogression. Recently, Branstator (1987) and Kushnir (1987) have presented statistical evidence of retrograding disturbances with periods of about three weeks.

The structure and evolution of the disturbances identified in the two studies is somewhat different, but they have common elements. In both studies, the most prominent features are the geopotential height anomalies of alternating sign in the Gulf of Alaska, which can be traced backward in time to western North America about a week earlier, and can be followed as they drift westward into eastern Siberia a week later. Branstator's results give the impression that individual anomaly centers can be followed through a complete cycle as they circle westward around the North Pole: his amplitudes in the Atlantic sector are not much smaller than those in the Pacific sector. Kushnir's results, on the other hand, indicate that the anomalies are much more geographically localized: they first appear over North America and drift westward until they decay over eastern Siberia. The reasons for the differences in these results are not clear at this point, but it is worth emphasizing that retrogression is a common element of the time evolution reported in both studies.

2.7 Local wavetrains vs. waves on latitude circles

In the previous sections we have made extensive use of one-point correlation maps to illustrate the structure and time evolution of high and low-frequency atmospheric variability. We have seen that the resulting patterns tend to be local in the space domain in the sense that they do not extend all the way around latitude circles. Since they are local in the space domain they are inherently nonlocal in the zonal wavenumber domain: i.e., more than a single zonal wavenumber is required to represent the structure and time evolution of such a pattern in a Fourier expansion. For example, the teleconnection patterns discussed in Section 2.5 are primarily composed of contributions from zonal wavenumbers m=1–4: the dipole patterns over the oceans in all four patterns (EA, WA, PNA, and WP) are mainly m=1, 2 while the downstream wavetrains over the continents in the EA and PNA patterns are mainly made up of m=3, 4 [see Fig. 3 of Nakamura et al. (1987).

From a mathematical point of view, a spectral decomposition of the atmospheric motion field is certainly as valid a representation as the maps that we have been using. Therefore, it is reasonable to question whether the reliance upon one point correlation maps has biased this presentation toward structures that are local in the space domain and nonlocal in the wavenumber domain.

We can put this question to rest by choosing a form of analysis which has a built-in bias toward pure zonal wavenumbers. If the resulting patterns are similar to the ones that we have already examined, then we can rest assured that they are real, and not simply a fabrication of the analysis scheme. A number of approaches are possible: following Wallace and Hsu (1983), we generate timeseries of the sine and cosine coefficients of 5-day mean[15] wintertime 500 mb height on the 50°N latitude circle for the first several zonal wavenumbers. The 50° latitude circle was chosen because it passes close to the centers of all the more prominent teleconnection patterns. The resulting timeseries $A_1(t)$, $B_1(t)$, $A_2(t)$, $B_2(t)$, etc, [where A and B denote cosine

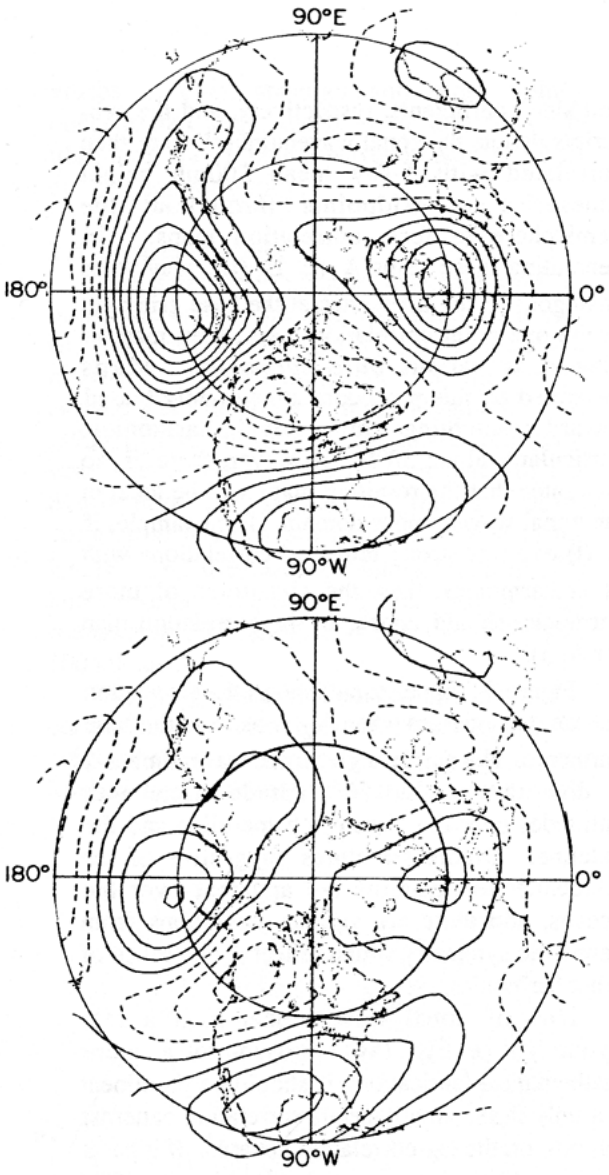

Fig. 32 Correlation maps for the cosine coefficient of zonal wavenumber 2 on the 50° latitude circle, referred to the Greenwich meridian, based on wintertime 5-day mean 500 mb height data. Upper panel: simultaneous. Lower panel: with hemispheric 500 mb height lagging A_2 by 5 days. See text for further explanation. After Wallace and Hsu (1983).

[15] The practice of replacing the daily data by consecutive 5-day (pentad) means serves as a "quick and dirty", lowpass filter, greatly reducing the amplitude of fluctuations with periods shorter than 7-10 days.

and sine coefficients, respectively, and the subscripts denote the zonal wavenumber] were then correlated with 5-day mean 500mb height timeseries at gridpoints throughout the hemisphere to form correlation maps. In generating these maps $A_1(t)$, $B_1(t)$.. play roles analogous to the timeseries at the base gridpoint in the one-point correlation maps: they may be viewed as various *base harmonics*. Maps generated by this procedure are certainly biased toward resembling pure zonal harmonics, particularly along 50°N. However, there is no guarantee that the resulting maps will be local in the zonal wavenumber domain. For example, if $A_1(t)$ exhibits strong temporal correlations with other harmonics, then the signatures of those harmonics should appear in the correlation map for $A_1(t)$.

Figure 32 (upper panel) shows the correlation pattern that emerges when A_2 is used as the base harmonic. Not surprisingly, zonal wavenumber–2 is dominant on the 50° latitude circle with antinodes near the Greenwich meridian and the dateline. Dipole structures suggestive of the teleconnection patterns are apparent over the oceans, and there are various deviations from geometric symmetry which reflect the presence of other harmonics.

Now if zonal wavenumber–2 is a real dynamical entity (as opposed to a mere mathematical fabrication), it should be prominent not only in the simultaneous correlation patterns, but also on the lag-correlation patterns. If it has a tendency to progress or retrograde along the 50°N latitude circle, that phase propagation should be readily apparent in the lag-correlation maps. The lower panel of Fig. 32 shows the correlation between A_2 and the 500 mb height field for the subsequent pentad. *It is apparent that zonal* wavenumber-2 hasn't fared very well over this 5-day interval. The Asian part of the pattern has almost disappeared and the part that remains more closely resembles the by now familiar PNA pattern than the wavenumber–2 pattern of five days earlier. Hence, the longitudinally localized patterns have prevailed, even though the analysis *scheme used in generating Fig 32 is biased* toward a pure zonal wavenumber–2 pattern. The simultaneous correlation pattern, which was rather local in the zonal wavenumber domain, evolves into a pattern which is local in the longitude domain. Other examples shown in Wallace and Hsu (1983) indicate that this behavior is rather typical: geographically local wavetrains tend to retain their identity longer than pure zonal wavenumbers. Further evidence of non-localness of the low frequency patterns in the zonal wavenumber domain is the fact that the temporal correlations between $A_1(t)$, $B_1(t)$, $A_2(t)$, etc. are quite strong; e.g., see Tables 1 and 2 in Wallace and Hsu (1983).

However, the Southern Hemisphere general circulation is a different story. Figure 33 shows a remarkably pure zonal wavenumber three pattern at higher latitudes, coupled with a zonal wavenumber six pattern at the lower latitudes. For another example, see Trenberth and Mo (1985). Such geometrically symmetric patterns are observed rarely, if ever, in monthly mean Northern Hemisphere maps, but they are not infrequently observed in the Southern Hemisphere. One point correlation maps for some gridpoints in the Southern Hemisphere show evidence of a zonal wavenumber three pattern [e.g., see Mo and White (1985)], and an eastward propagating zonal wavenumber–5, with periods on the order of 10 days, also plays a prominent role in the transient variability [Salby (1982)].

Fig. 33 Mean 500 mb map for the Southern Hemisphere for the period 6 July—4 August, 1981 based on the ECMWF analysis for that day. Contour interval 60 m. After Wallace and Hsu (1983).

It is likely that the more extensive mountain barriers in the Northern Hemisphere, which are responsible for concentrating the jetstreams and stormtracks into well defined longitudinal sectors, account for much of the lack of geometrical symmetry of the Northern Hemisphere transient planetary waves.

Patterns with a strong contribution from a single zonal wavenumber are observed in the high latitude, winter stratospheres of both hemispheres, with zonal wavenumber one or two usually being dominant.

The ideas put forth by Charney and Drazin (1961), generalized to two dimensions, provide a theoretical basis for interpreting these rather striking differences between the structure of the low-frequency variability in the Northern and Southern hemispheres and between the northern winter troposphere and stratosphere. In the presence of a given amount of superrotation ω, of the atmosphere, relative to the earth's rotation rate Ω, the two–dimensional wavenumber n whose westward phase propagation due to the beta-effect just balances the eastward advection due to the zonal flow is given by

$$n(n+1) = 2\,(1 + \Omega/\omega)$$

Wavenumbers adjacent to this quasi-stationary wavenumber should play a prominent role in the low frequency variability. It is evident that n is highly sensitive to the relative amount of superrotation ω / Ω. This ratio tends to be larger in the Southern Hemisphere winter troposphere than in the Northern Hemisphere winter troposphere because the westerlies in the 40–60°S latitude belt are about 50% stronger. It follows that, $n \approx 4$–5 in the Southern Hemisphere, compared to around 6 in the Northern Hemisphere. The Southern Hemisphere polar vortex is also somewhat more tightly concentrated about the pole than its Northern Hemisphere counterpart, so that the scale of the low-frequency planetary waves is considerably larger relative to the scale of the polar vortex itself in the Southern Hemisphere than it is in the Northern Hemisphere; i.e., the Southern Hemisphere planetary waves are characterized by a narrower spectrum of Fourier components on latitude circles, and they don't have as much space in which arrange themselves so as to be geographically local. The stratospheric polar vortex is even stronger and more tightly concentrated about the pole so that only the ultra-long waves [zonal wavenumbers 1 and 2] can be quasi-stationary.

2.8 Vertical structure

Consistent with their interpretation as baroclinic waves, the high frequency transients tilt westward with height by approximately a quarter of a wavelength between the earth's surface and the 500 mb level [Wallace et al. (1988)]. The situation for the lower frequency transients is more complex: over much of the hemisphere the shapes of the one-point correlation patterns are much the same at all levels [i.e., they are *equivalent barotropic*[16]] but in some localized regions they exhibit remarkable differences between the 1000 and 500 mb levels.

Fig. 34 gives a hemispheric survey of the correlation coefficient between 1000 and 500 mb height at the same gridpoint, based upon lightly lowpass filtered wintertime data. In regions such

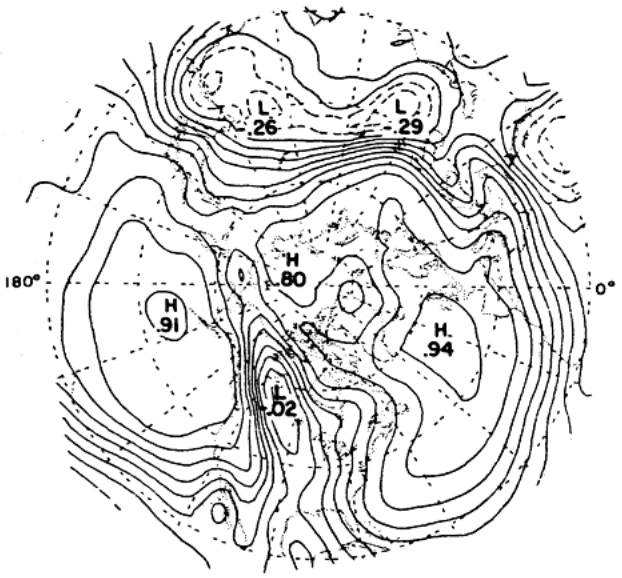

Fig. 34 Correlation coefficient between lowpass filtered 1000 and 500 mb height at the same gridpoint during Northern winter. The filter has a half-power point around 10 days. Based on Blackmon et al. 1979.

16 A three-dimensional structure in which the horizontal and vertical structures are separable [i.e., the amplitude of the geopotential height perturbations may vary with height, but not the shape of the pattern] is referred to as *equivalent barotropic*, a term borrowed from the earlier literature on numerical weather prediction.

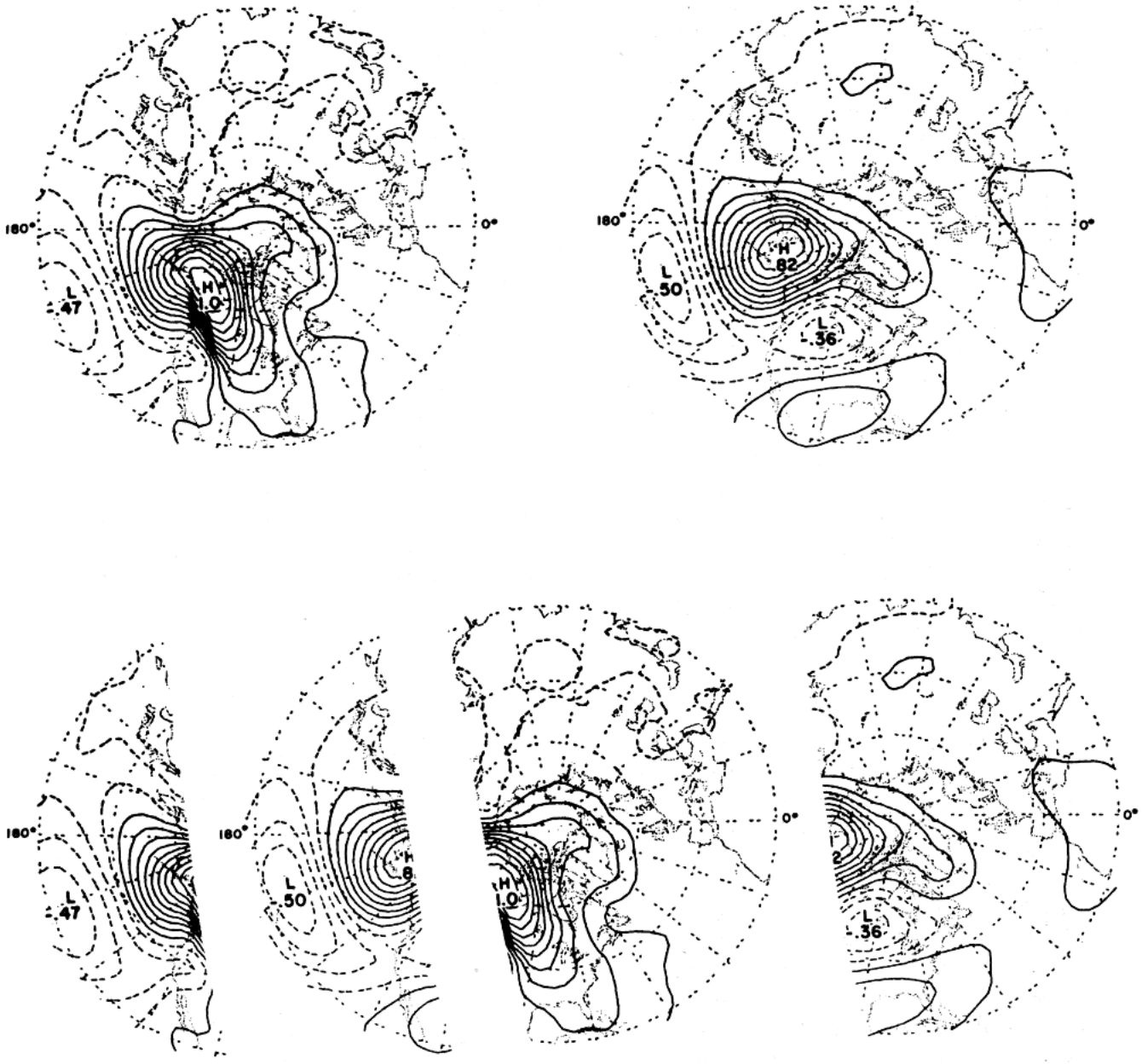

Fig. 35 One-point correlation maps based upon the time series of 1000 mb height at the base gridpoint [62.5°N, 130°W): *(upper left)* 1000 mb height; *(upper right)* 500 mb height. Based upon consecutive 5-day mean wintertime data from which the climatological mean annual cycle has been removed. After Hsu and Wallace (1985). *Partial maps at lower–left:* as in upper maps, but for the region to the west of the Rockies. *Partial maps at lower–right:* as in upper maps, but for the region to the east of the Rockies.

as the eastern oceans, where the correlations are strong, the low frequency fluctuations exhibit a barotropic structure, whereas in regions where the correlations are weak, the structure is more baroclinic. The continental regions to the north and east of the Rockies and Himalayas are notable for their weak and even negative correlations. Note that in regions in which 1000 and 500 mb height fluctuations tend to be out of phase, the thickness fluctuations tend to be larger than the geopotential height fluctuations and surface anticyclones tend to be cold and cyclones warm: in these regions pressure fluctuations of a given amplitude tend to be accompanied by larger temperature fluctuations than in regions of strong positive correlations.

Fig. 35 shows representative one-point correlation maps for one of these regions. Both panels are based upon wintertime, lowpass filtered 1000 mb height data for the base gridpoint [62.5°N, 130°W]. It is evident that some of the features in the 500 mb height pattern are displaced far to the west of their counterparts in the 1000 mb height patterns. The relationship between the patterns at the two levels becomes clearer when one looks separately at the regions to the west and east of the Rockies, as shown in subsequent panels of Fig. 35. To the west of the Rockies, where strong positive correlations prevail in Fig. 34, the patterns in Fig. 35 are very similar at the two levels. To the east of the Rockies, where the correlations in Fig. 34 are

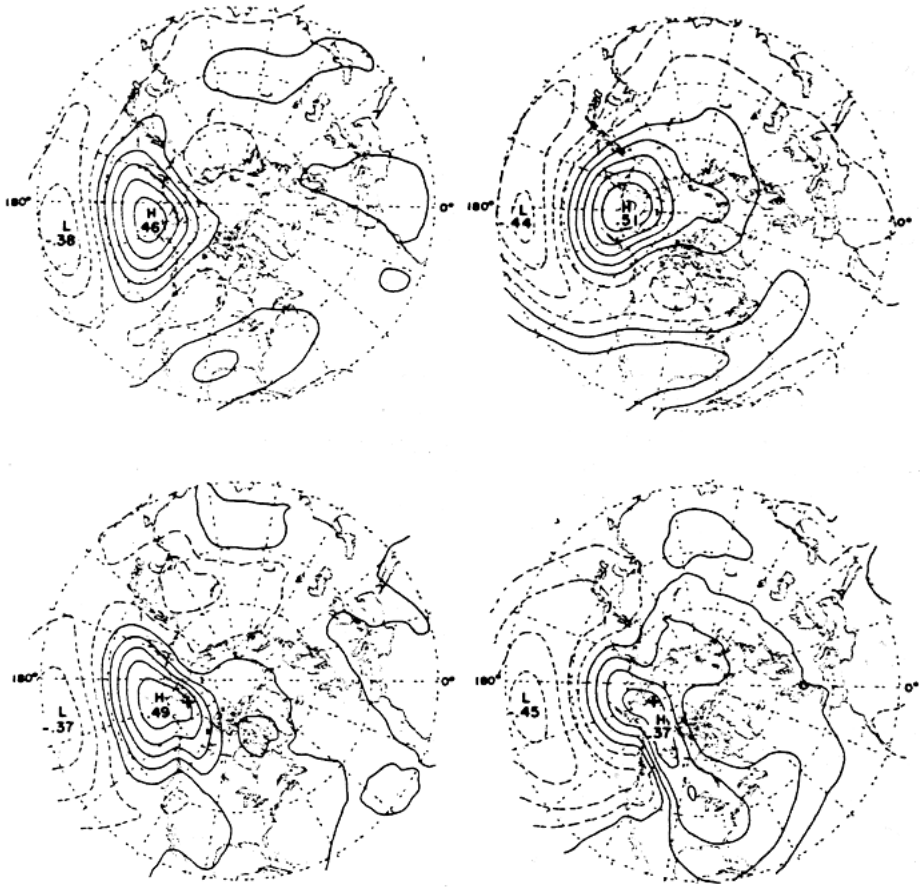

Fig. 36 Lag correlation maps based on a time series very similar to the one used as a reference time series for the previous figure. Upper panels are 500 mb height and lower panels are 1000 mb height. The panels on the left are for 5 days earlier than the reference time series and the panels on the right are for 5 days later than the reference time series. By comparing left and right panels, one can see the evolution of the patterns at the two levels. After Hsu and Wallace (1985).

much weaker, the structure of the patterns in Fig. 35 is much more baroclinic. Features in this region exhibit a strong northwestward tilt with height, with a phase shift of more than a quarter wavelength between the 1000 and 500 mb levels.

The nature of these patterns is revealed more clearly by the lag-correlation maps shown in Fig. 36. From these maps it is evident that the evolution of the features at the two levels is very different. At the 1000 mb level there is clear evidence of southeastward phase propagation along the lee slopes of the Rockies. This behavior appears to be confined to the lowest levels of the atmosphere. The sequence at the 500 mb level is qualitatively similar to that revealed by the examples shown in Fig. 29., with energy dispersion through geographically fixed wavetrains.

Newton (1956) and more recently Wallace and Hsu (1985) and Hsu (1987) argue that the phase propagation at the lower levels is due to the "equivalent beta-effect" associated with the terrain slope. For example, a surface anticyclone situated along the eastern slopes of the Rockies, say over Montana, induces a northeasterly flow to the southeast of it, over Wyoming and Colorado. This flow has a strong upslope component, which induces divergence in the free atmosphere. It acts as a source of anticyclonic vorticity to the southeast of the anticyclone. In a similar manner, the westerly flow over the Canadian province of Alberta has a strong downslope component, which induces low-level convergence, which acts as a source of cyclonic vorticity. This source/sink couplet associated with the upslope and downslope flow causes the low-level vorticity minimum over Montana and the associated anticyclone in the pressure pattern to propagate southeastward along the lee slopes of the Rockies. The same arguments could be invoked to explain the southeastward propagation of a cyclone. In this mechanism, the terrain slope plays a role analogous to the variation of the Coriolis parameter with latitude [i.e., the β-effect] in causing disturbances to propagate. Whereas the β-effect always causes disturbances to propagate westward relative to the steering flow in which they are embedded, it is evident that the terrain slope induces a propagation along contours of constant surface elevation, with higher terrain to the right in the Northern Hemisphere. It causes disturbances to propagate anticyclonically around regions of elevated terrain, such as the Rockies, the Tibetan plateau, and Greenland.[17]

The importance of this "equivalent β-effect" depends upon the degree to which the disturbances are trapped in the lower troposphere. If they are not strongly trapped, the divergence associated with a given amount of upslope flow will be distributed through a relatively deep layer, and therefore it will not be very strong. On the other hand, if the disturbances are strongly trapped near the earth's surface, the divergence will be large enough to exert a strong control upon the evolution of the sea-level pressure pattern. The degree to which disturbances are trapped in the lower troposphere increases with the ambient static stability. Hence, this phenomenon is more pronounced along the lee slopes of the Rockies than over the windward slopes.

The regions of low correlation between 1000 and 500 mb height fluctuations in Fig. 34 appear to be related to the type of pattern illustrated in Figs. 35 and 36, which is prominent along the lee slopes of the Rockies and to the north and east of the Tibetan Plateau. Elsewhere, the low frequency fluctuations exhibit a vertical structure with only a very modest westward phase shift from the earth's surface up to the 500 mb level. Hence, it can be argued that in regions remote from large mountain ranges, the dynamical processes responsible for the observed low frequency variability during the northern winter are, to first order, barotropic in character.

2.9 Interaction with the time-mean flow

In Section 2.3 it was shown that the low frequency transients transport westerly momentum eastward in the climatological mean jet exit regions over the mid-oceans, where $\overline{u'^2} >> \overline{v'^2}$. This behavior is illustrated by the extended Eliassen-Palm flux diagnostic shown in Fig. 17. The signature of this down-gradient momentum flux is particularly striking for the

[17] The importance of the equivalent β-effect associated with terrain slope is widely recognized in the oceanographic literature. Waves that propagate along the terrain slope due to this effect are called *shelf waves*. They are not to be confused with the so-called *coastal Kelvin waves* or *edge waves*, which are characterized by flow along (not across) terrain contours. For further discussion, see Rhines (1970) and Mysak (1980).

very low frequency transients that are resolved by monthly mean data (Fig.17d). Evidently, the horizontal structure of these very low frequency transients is conducive to extracting kinetic energy from the climatological mean flow.

The high temporal variance of the zonal wind component in the jet exit regions is, in turn, related to the variability associated with the Pacific/North American (PNA) and Eastern Atlantic (EA) teleconnection patterns described in Section 2.5. As the polarity of the geopotential height anomalies associated with these patterns switches back and forth, the zonal wind in the jet-exit regions undergoes large fluctuations in strength. For example, when geopotential heights are below normal over the northern oceans and above normal in the subtropics, zonal winds in the jet-exit regions are stronger than normal; i.e., the jetstreams extend farther to the east into the mid-oceans than they do in the climatological mean. Conversely, when the height anomalies are of opposite sign, zonal winds are weaker than normal in the mid-oceans; i.e., the jetstreams are retracted relative to their climatological mean positions. In the time average over one or more ideaized "cycles" consisting of alternating positive and negative zonal wind anomalies in the jet exit regions, these transients transport westerly momentum eastward, out of the climatological mean jetstreams and into regions of relatively weaker climatological mean zonal winds. Through these transports, they tend to weaken the longitudinal contrasts in zonal wind, thereby reducing the amplitude of the zonally asymmetric component u^*, which accounts for most of the kinetic energy associated with the stationary waves. The energy lost by the stationary waves is gained by the zonal wind component associated with the low-frequency transients.

Nakamura et al. (1987) have shown that all the teleconnection patterns described in Section 2.5 are associated with an energy conversion in the sense described above, but that the PNA and EA patterns are associated with by far the largest conversions because they are ideally situated with respect to the jet-exit regions, as illustrated in Fig. 37. We will now show that these two patterns appear to have some special significance, not only from the point of view of kinetic energy conversion, but also as normal modes associated with barotropic instability of the zonally varying climatological mean flow.

2.10 The possible role of barotropic instability

Simmons (1982) and Simmons et al. (1983) performed a number of numerical experiments with a simple model based upon the barotropic vorticity equation on a sphere. The "source" term associated with the horizontal divergence is specified such that it exactly balances the vorticity advection associated with the climatological mean, January 300 mb flow. Hence, if the model is initialized with this flow, it will remain in a steady state. Figures 38-40 show a series of snapshots from three different runs with this model. In each of the runs the initial conditions consist of the usual January climatological mean 300 mb streamfunction plus an arbitrarily small perturbation, elliptical in shape and essentially confined to a localized region 30° of latitude by 30° of longitude in extent. The perturbations in the model flow

---

Fig. 37 Schematic illustration of the dominant centers of action of the PNA and EA teleconnection patterns, in relation to the wintertime climatological mean jetstreams, indicated by the heavy arrows. After Blackmon et al. (1984).

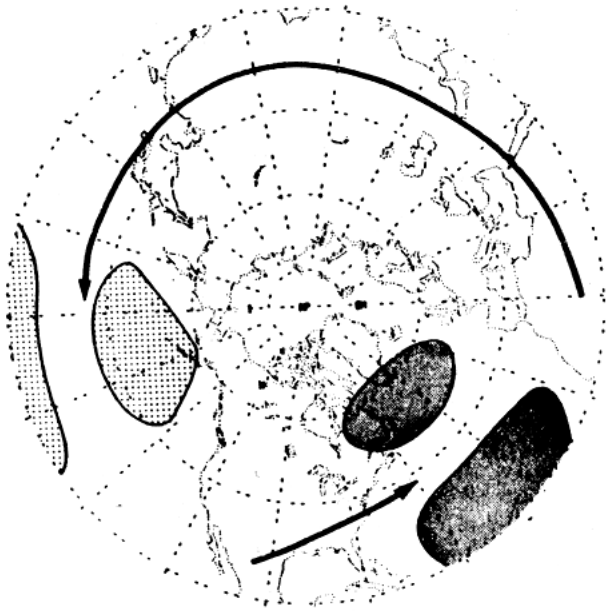

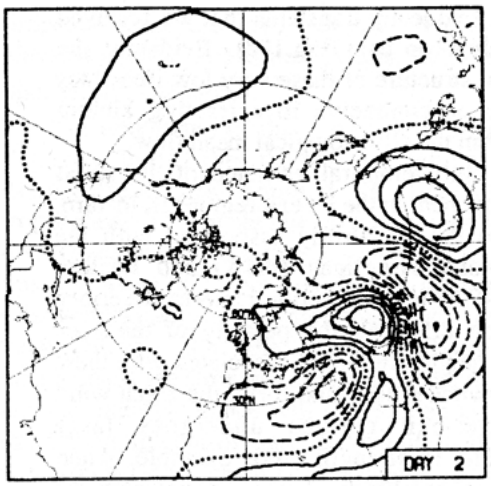

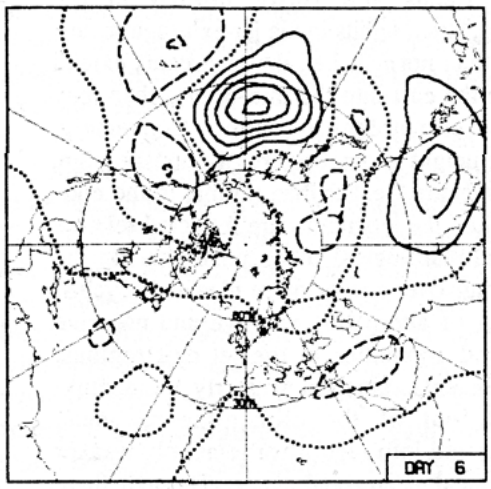

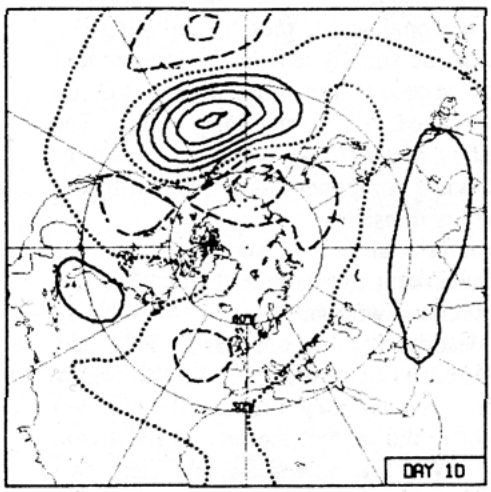

Fig. 38 Perturbation streamfunction at Days 2, 6, and 10 for an initial disturbance centered at 30°N, 0°E. The contour interval is 1/30 of the initial maximum amplitude. The zero contour is dotted. After Simmons et al. (1983).

---

field are subject to a linear damping with a 5-day *e*-folding time.

Figure 38 shows results for an initial perturbation centered on the Greenwich meridian at 30°N, near Gibraltar. Over the first two days this disturbance disperses into a train of waves which, at Day 2, is much as would be anticipated on the basis of results of Hoskins et al. (1977), with an eastward movement and weakening of the initial center, a bowing and splitting of the ridge formed immediately downstream of it, and a generally equatorward bias to the wave propagation. Dispersion and dissipation continue beyond Day 2 such that by Day 6 only one major center, located just to the west of the Dateline remains.

A significant change occurs between Days 6 and 10. The major center over the Pacific moves slowly eastward without loss of amplitude, with negative centers established to its south, over northeastern Siberia and over western North America. A positive center develops over the southeastern United States. Note that the pattern at Day 10 is similar to the PNA teleconnection pattern.

The solution of a second initial value problem is illustrated in Fig. 39. In this case an initial negative perturbation is centered at 30°N,120°E. The Day 2 pattern shows a more pronounced poleward component of the initial dispersion than in the preceding example, and the largest positive region at this time is located close to the position of the largest disturbance at Day 6 in the earlier case. By Day 6 the perturbation is very similar in structure to the Day 10 result shown in Fig. 38, though its amplitude is larger. By Day 10 in this second case, the amplitude of the perturbation has diminished, but there has been little change in the wave pattern, except over the Atlantic.

Fig. 39 As in Fig. 38 but for an initial perturbation centered at 30°N, 120°E.

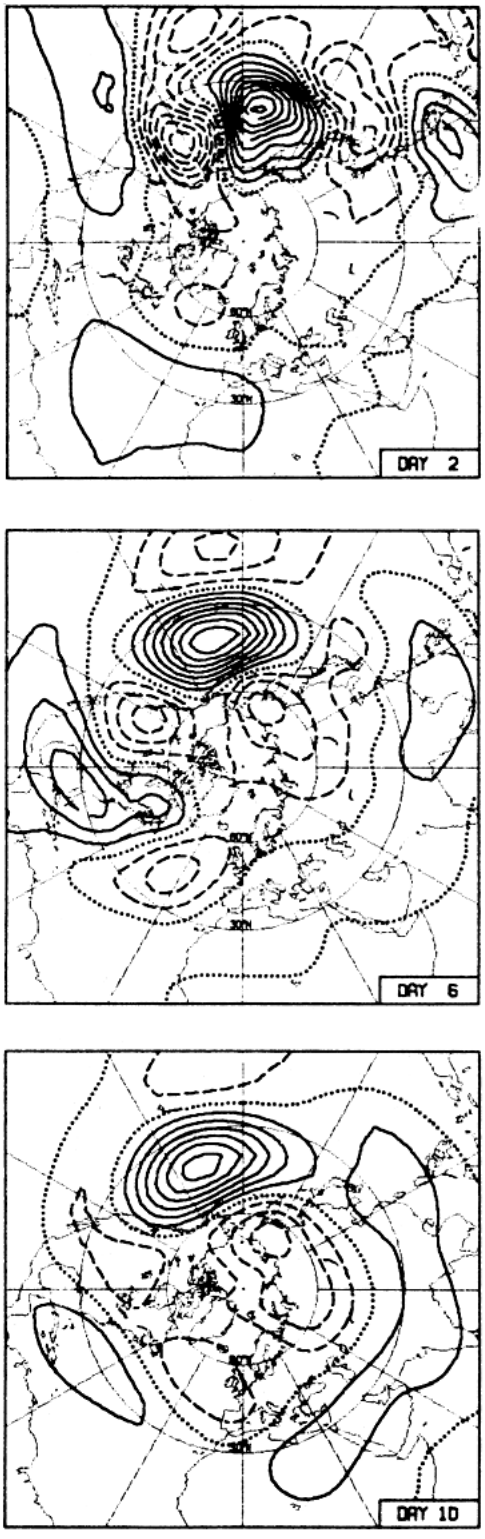

Fig. 40 As in Fig. 38 but for an initial perturbation centered at 15°N, 90°W.

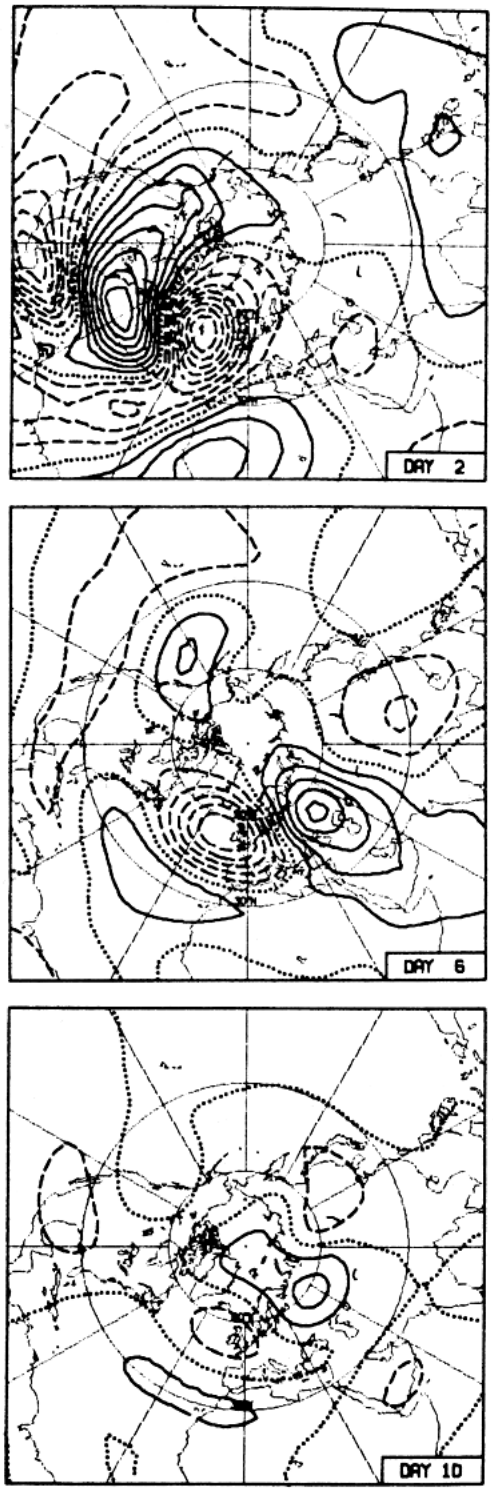

Although the two cases illustrated in Figs. 38 and 39 were chosen on the basis of the relatively large amplitudes of what it is tempting to call the model's "PNA pattern", Simmons et al. observed a tendency for this pattern to recur repeatedly (with either polarity) in their experiments, in which a wide variety of initial conditions was employed. In most of their experiments it became the dominant pattern at Day 6 and beyond. However, in a few of their experiments a second pattern, centered in the Atlantic, became dominant. Figure 40 shows a sample initial value calculation in which the initial vorticity perturbation was located at 15°N, 90°W, near Central America. The response at Day 6 and beyond clearly resembles the EA pattern, but the amplitudes are not as large as those over the Pacific in the previous two figures.

In the sample integrations shown in Figures 38-40, the linear drag gradually reduces the amplitude of the perturbations about the climatological mean steady state. However, when the linear drag is reduced so that its *e*-folding time is longer than about a week, the disturbances are observed to amplify as a result of the fact that the climatological mean January 300 mb flow is barotropically unstable. By

(1) setting the linear damping equal to zero,

(2) setting the amplitude of the initial perturbations many orders of magnitude smaller than the climatological mean stationary waves, and

(3) letting the disturbances amplify by several orders of magnitude before examining them,

one can recover the fastest growing normal mode associated with these amplifying disturbances. Over the course of such a long integration, the fastest growing normal mode has sufficient time to amplify much more than any of the other modes so that the solution converges to it, regardless of the form of the initial perturbation. One can be assured that this will eventually happen, provided that the first and second modes have different growth rates. Since the perturbations remain very small throughout the time integration, the calculations are essentially linear.[18]

The normal modes are of the general form

$$e^{\sigma t}\,[\,A(\lambda,\theta)\sin\omega t + B(\lambda,\theta)\cos\omega t\,]$$

The kinds of normal modes that most of us are accustomed to dealing with are characterized by simple wavelike structures in the longitude domain so that A and B can be expressed in the form $F(\theta)\cos k\lambda$ and $F(\theta)\sin k\lambda$, respectively, where F is an arbitrary function of latitude. It is readily verified that these solutions assume the form of zonally propagating wave disturbances. In the more general case it is not required that A and B have any special analytic form or interrelationship.

Figure 41 shows a series of "snapshots", 4–5 days apart from one of these long integrations. The value of σ is such that the e-folding time for these amplifying disturbances is 6.8 days. In order to simplify the figure, the contour interval has been adjusted in each panel so as to exactly compensate for the growth. With this adjustment, the normal mode solutions should be perfectly periodic, with period $2\pi/\omega$.

The 22-day period covered in Fig. 41 takes us just about exactly halfway through the 45-day period of the fastest growing normal mode. Concentrating attention first on Day 178 (upper left) we note the weak positive center over the dateline near 35°N. During the next few days of the integration this center drifts slowly eastward and grows in amplitude to give the pattern shown at Day 183 (upper right). Over the same time interval there is a decay of the relatively zonal perturbation over the Atlantic, whose structure qualitatively resembles the observed correlation patterns in that sector of the hemisphere. Beyond Day 183 the Pacific center is the dominant feature on the map, growing more or less in situ, followed by negative and positive centers downstream over North America and the western Atlantic. A negative center also develops near Iceland, and becomes the dominant feature as the Pacific center weakens beyond Day 191 (middle right). Thus by Day 200 (bottom right) the pattern is almost the complete reverse of that shown for Day 178. Over the Pacific, the negative center to the south of what was the major positive center has moved westward to the dateline, from which position it will move eastward and amplify beyond Day 200

[18] The structure and behavior of the most unstable normal mode as deduced from the extended linear time integration, were verified by obtaining the solutions to the eigenvalue problem by a matrix technique.

Fig. 41 The streamfunction of the most unstable mode in the numerical model of Simmons et al. (1983) at selected days within one half cycle of its oscillation. The contour interval is arbitrary.

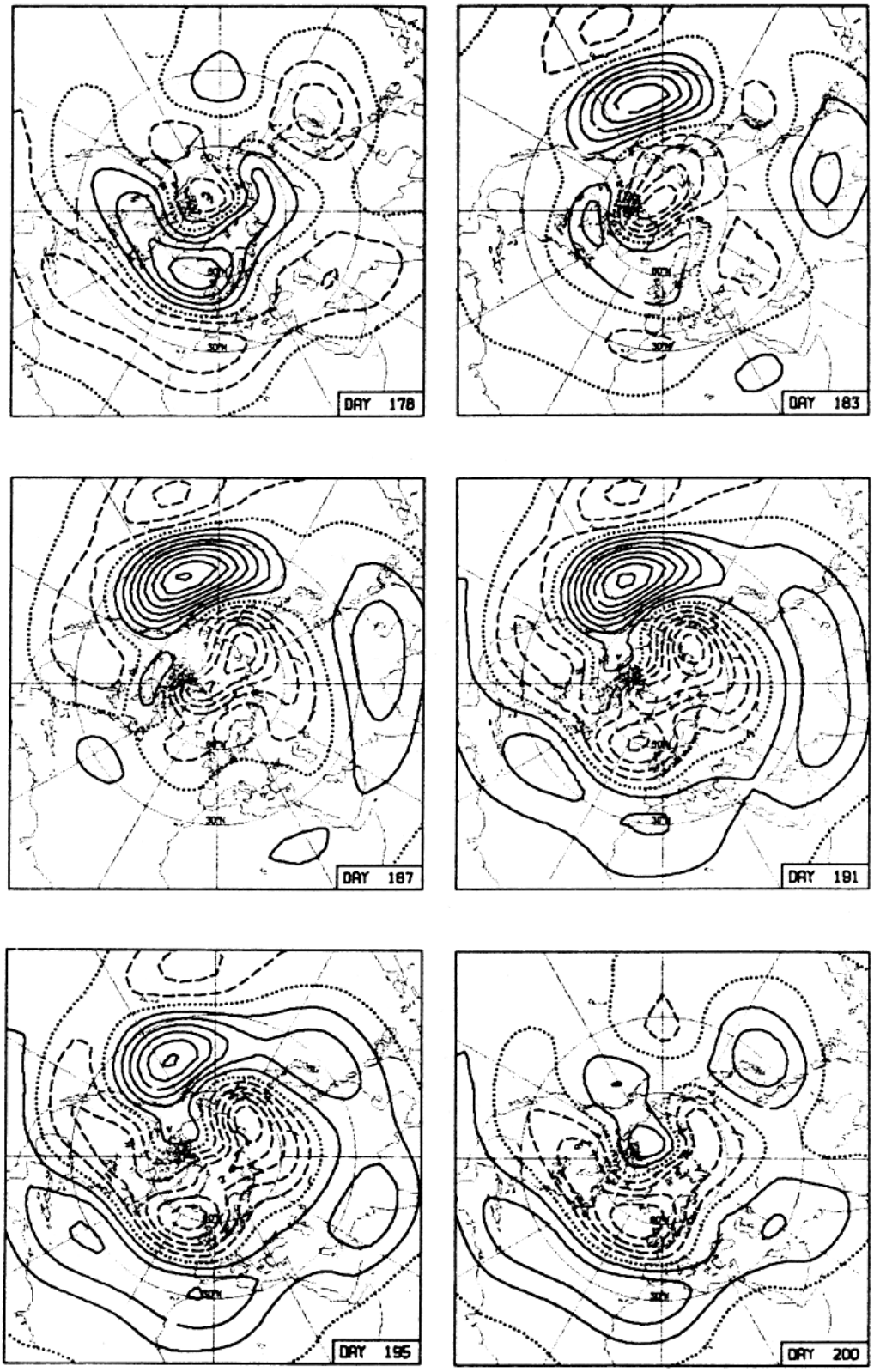

as the normal mode pattern repeats itself with reversed sign.

The interaction between this fastest growing normal mode and the mean flow can summarized concisely by showing the distribution of the extended Eliassen-Palm flux produced by these perturbations as they evolve through a single 45-day cycle. In order to make the results independent of the phase in which the cycle begins and ends, the exponential growth is

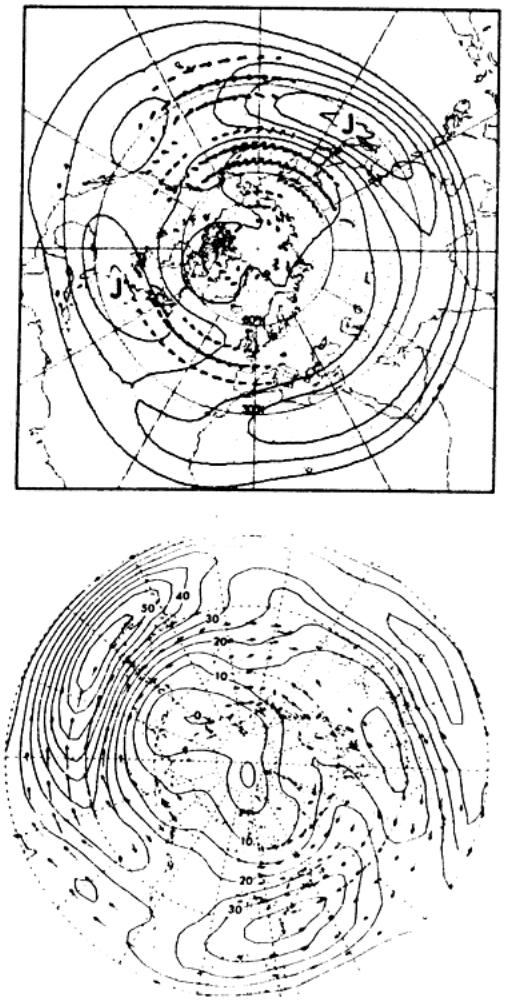

Fig. 42 *(upper panel)* The extended Eliassen-Palm flux E averaged over one cycle of the most unstable mode and superimposed upon isotachs of the zonal velocity component of the climatological basic state. The contour interval is 10 m/s, and jet maxima are indicated by the symbol J (printed sideways). The scaling of the arrows denoting the flux vector is arbitrary. After Simmons et al., (1983). *(lower panel)* Fig. 17d repeated, based upon observations.

suppressed, as in Fig. 41. The resulting pattern, shown in Fig. 42a bears a remarkably strong resemblance to the corresponding distribution for the observed low-frequency transients shown in Fig.17d and repeated in Fig. 42b.

Hence, there is strong observational evidence linking the PNA and EA teleconnection patterns with the fastest growing normal mode associated with the barotropic instability of the climatological mean flow. In view of the 2-3 day *e*-folding times associated with baroclinic instability, it may be difficult to understand how barotropic instability, with its much longer (6.8 day) *e*-folding time, could exhibit such prominent signatures in the low-frequency variability. This result is less surprising when one takes into account the fact that over certain periods during the cycle descibed in Fig. 41, the local growth rate of the disturbances in the Pacific is up to about three times as large as the average growth rate for the mode as a whole. Furthermore, it is worth keeping in mind that baroclinic waves exhibit a distinct life cycles in which the growth phase is followed by an equally rapid, nonlinear decay phase [see Simmons and Hoskins (1978)]; hence, the faster growing wave is not necessarily the one that will attain the largest amplitude. It should also be noted that the filters used in isolating the low-frequency variability strongly suppress the variance associated with baroclinic waves, which exhibit periods shorter than a week.

On the other hand, lest the importance of barotropic instability be overemphasized relative to baroclinic instability, it should be noted that there is no observational evidence that the PNA and EA patterns appear in quadrature, as suggested by the sequence in Fig. 41. These patterns seldom appear in anything resembling a pure form on synoptic charts or even on time-mean maps: they are apparent only in statistical ensembles. They account for only a modest fraction of the variance of the geopotential height field. [The corresponding normal mode structures associated with baroclinic instability regularly appear in quadrature with one another, in agreement with theory, as evidenced by the systematic eastward propagation of these disturbances. They are frequently evident on conventional synoptic charts and they account for most of the variance of the high frequency fluctuations.] Furthermore, as will be discussed

Fig. 43 Distributions of the 300 mb height tendencies associated with the fluxes of vorticity by the transients during wintertime for *(a)* bandpass (2.5-6-day period) and *(b)* lowpass (>10-day) filtered NMC data. The interval between solid contours is 5 x 10^{-4} m^2 s^{-3}, which correponds to roughly 5 m of geopotential height per day. Arrowheads indicate the direction of of the associated acceleration of the geostrophic wind. After Lau and Holopainen (1984).

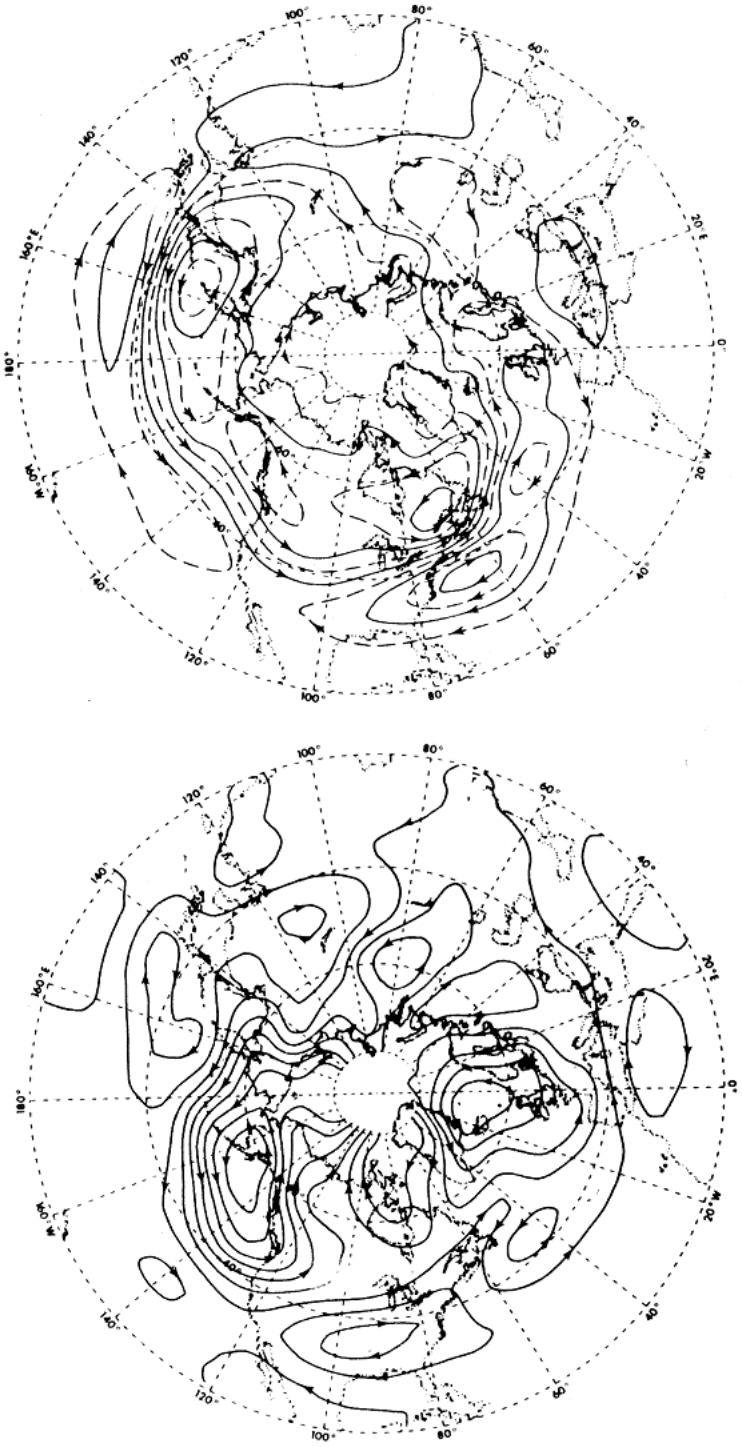

in Brian Hoskins' lectures, there are unresolved ambiguities concerning the nature of barotropic instability and its relation to the forcing of the climatological mean stationary waves.

2.11 Forcing of the mean flow by the transients

It is of interest to determine whether the signature of any of the dynamical processes described in the previous sections is recognizable in the net forcing of the time-mean flow by the transients Lau and Holopainen (1984) have shown that the quasi-geostrophic tendency equation for the time-mean flow provides a convenient framework for inferring the net effect of the horizontal fluxes of momentum and heat by the transients, taking into account the ageostrophic circulations that they induce. In this formulation, the convergence of the eddy fluxes plays a role analogous to the advection terms in the instantaneous tendency equation [e.g., see Holton (1979), p.131].

Figure 43, from Lau and Holopainen (1984), shows the 300-mb geopotential height tendencies induced by the vorticity fluxes associated with high- and low-frequency fluctuations as defined earlier. The contour interval between solid contours is roughly equivalent to 5 m (of 300-mb height) per day. Calculations are based on the NMC data set for Northern Hemisphere winter. The vorticity fluxes by the high-frequency transients (Fig. 43a) tend to accelerate the climatological mean jetstreams along their northern flanks. Throughout the Pacific and American sectors of the hemisphere, the transients induce westerly accelerations in the 40°-50°N latitude belt. The low-frequency transients (Fig. 43b) produce stronger accelerations of the mean flow, particularly over the eastern oceans (note that the contour interval is effectively double that in Fig.43a). They tend to weaken the longitudinal contrasts in jet stream structure, accelerating the zonal flow where it is weak over the eastern Pacific and Europe, decelerating the Asian jet stream southeast of Japan, and shifting the jet streams over the western United States and North Africa poleward, bringing them more closely into line with the other jets.

The corresponding tendencies that result from the heat fluxes associated with the transients (not shown here) play an important role in forcing the surface westerlies in the 40°-50°N latitude belt, but they play only a minor

role in forcing the 300 mb height tendencies. The total 300-mb height tendency induced by the fluxes of heat and vorticity associated with the transients, shown in Fig. 44, closely resembles that associated with the vorticity flux induced by the low-frequency transients alone (Fig. 43b). Hence, it is apparent that low-frequency barotropic processes dominate the wave-mean-flow interaction at the jet stream level.

Hoskins et al. (1983) have shown that to within about 10%, the barotropic component of the forcing of the mean zonal flow by the transients is given by the horizontal divergence of the Eliassen-Palm flux vector $\boldsymbol{E}$. From a comparison of Figs. 17a and 44 it can be seen that all the features described in the preceding paragraph correspond to well-defined regions of divergence or convergence in the $\boldsymbol{E}$ field. Hence the patterns in the $\boldsymbol{E}$ vectors are helpful in interpreting the net forcing of the mean zonal flows by the transients at the jet stream level. Not included, however, is the effect of the diabatic heating associated with the high

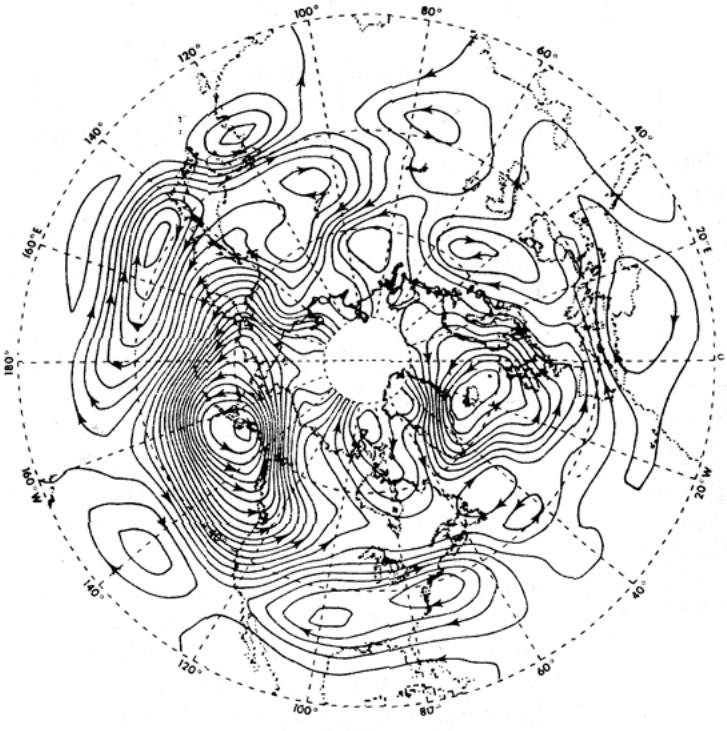

Fig. 44 Distribution of wintertime 300 mb geopotential height tendencies associated with the sum of the vorticity and heat fluxes by the transients, based on unfiltered NMC data. Contour interval 5 x 10^{-4} m^2 s^3. Arrowheads indicate the direction of the associated acceleration of the geostrophic wind. After Lau and Holopainen (1984).

frequency transients in the stormtrack regions. Brian Hoskins will argue in his lectures that this effect may be of comparable or even greater importance than those considered here.

The forcing of the low-frequency transients by baroclinic waves was touched upon at the beginning of this section in the discussion of MacVean's numerical simulations. Recent observational studies by Mullen (1986) and Lau (1988) show evidence of a strong relationship between the stormtracks and the time-mean flow upon which they are superimposed. The relationship is such that the vorticity fluxes by the baroclinic waves tend to reenforce whatever asymmetries are present in the mean-flow.and (in Mullen's results) to cause large amplitude blocking anticyclones to retrograde. As in Lau and Holopainen's results, the vorticity fluxes tend to be more important than the heat fluxes, whose effects are largely dissipative. Numerical simulations by Shutts (1983, 1986) with idealized flow patterns in a barotropic model provide a basis for a qualitative understanding these results.

2.12 Summary and concluding remarks

The foregoing observational results provide an observational basis for distinguishing three distinct types of transient variability, in terms of the frequency range in which they occur, as summarized in Table 1.

High frequency variability [periods shorter than a week] is dominated by wavelike disturbances organized in the form of zonally oriented wavetrains. The largest amplitudes and the strongest organization are observed in zonally elongated bands located slightly poleward and downstream of the climatological mean jetstreams. The perturbations in the geopotential height field associated with these disturbances are elongated in the meridional direction, so that the meridional wind component in the waves tends to be stronger than the zonal component. Their wavelength is on the order of 4000 km [zonal wavenumber 8]. They propagate with a phase speed comparable to the 700 mb flow and they tilt westward with height. They feed energy into the barotropic component of the climatological mean flow and the low-frequency transients. These characteristics all support an identification of the high frequency fluctuations as baroclinic waves.

The intermediate frequency (10-30 day

period) variability also exhibits some degree of organization in the form of zonally oriented wavetrains in which the geopotential height perturbations are elongated in the meridional direction. Wavelengths are on the order of 7000 km (zonal wavenumber 4-6); long enough for the β effect to cancel much of the eastward phase speed due to the advection by the mean wind.

The primary waveguides are as illustrated in Figure 45. they cut across the climatological mean jetstreams from the poleward side at the upstream end to the equatorward side on the downstream end. The dominant form of evolution is through the dispersion of energy through stationary wavetrains, as evidenced by the development of new centers on the downstream end of the wavetrain and the decay of old centers on the upstream end. It is distinct from the phase propagation associated with the high frequency transients.

The low-frequency (>60 day period) variability is largest over the mid-oceans downstream of the climatological mean jetstreams. In these regions, the low-frequency fluctuations are strongly anisotropic, with the zonal wind component being much stronger than the meridional component. The corresponding geopotential height fluctuations in these regions are characterized by north-south dipole patterns straddling the jet exit regions. Perturbations with such a shape are capable of extracting kinetic energy from the climatological mean flow through the barotropic energy conversion term $-\overline{u'u'}\partial\bar{u}/\partial x$. In this sense their function in the Lorenz kinetic energy cycle is opposite to that of baroclinic waves, as illustrated in Fig. 46. By transporting westerly momentum eastward through the jet exit regions, they act to smooth out the longitudinal asymmetries in the climatological mean wind field. The low frequencies prevail in determining the sign of the total conversion of kinetic energy between the climatological mean flow and the transients.

The low-frequency variability exhibits some tendency for geographically fixed "teleconnection patterns"which can be isolated by means of rotated principal component analysis or through the analysis of the "teleconnectivity field" as described in Section 2.5. The PNA and EA patterns are situated in favored geographical locations for extracting kinetic energy from the climatological mean jetstreams. In addition to the patterns described in Section 2.5, two other patterns are worthy of note. The so-called North Atlantic Oscillation (NAO) identified by Walker and Bliss (1932) and documented in detail by van Loon and Rogers (1978) appears to be an

TABLE 1 Summary of the properties of the atmospheric variability in three different frequency bands in extratropical latitudes.

Frequency band	*High*	*Intermediate*	*Low*
Period	< 7 day	10–30 day	.> 60 day
Wavelength	4000 km	7000 km	>10,000 km
Zonal waves	6–9	4–6	1–4
Anisotropy	u < v	u < v	u > v
Organization	wavetrains	wavetrains	N–S dipoles
Evolution	eastw'd prop.	stationary	stationary
Interpretation	baroclinic waves	Rossby-wave dispersion	unclear

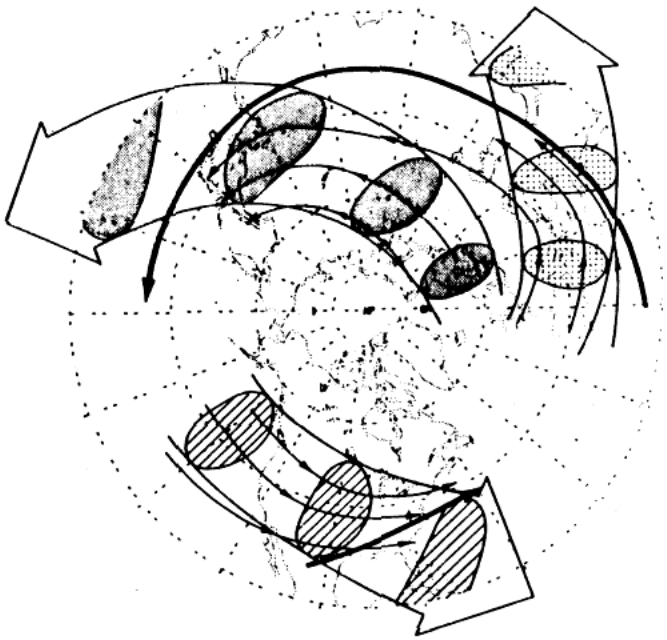

Fig. 45 Idealized model of the mode of organization of the intermediate frequency (10–30 day period) fluctuations showing the preferred three preferred waveguides deduced from analysis of the teleconnectivity map, one-point correlation maps, and rotated principal components. The shaded "centers of action" are shown only for the purpose of indicating the shapes, wavelengths and orientations of the disturbances within those waveguides; they are not intended to indicate geographically fixed patterns. After Blackmon et al. (1984a).

important mode of variability in the Atlantic sector. The manifestations of this pattern at the 500 mb level resemble the WA pattern, but the centers of action are centered about 10° of latitude farther to the north. The pattern shown in Fig. 35 is closely related to the North Pacific Oscillation identified by Walker and Bliss (1932) and discussed more recently by Rogers (1981). Several additional patterns have been pointed out in the literature cited in Section 2.5 and in other references cited by Barnston and Livezey (1987), but I will not take the time to discuss them here.

Many of the results presented in this section and summarized in Table 1 have been confirmed in a recent observational study by Schubert, who examined the structure and evolution of the leading (unrotated) eigenvectors of the time-filtered, wintertime 500 mb height field, using a carefully designed set of filters which distinguish between five different frequency subranges (as opposed to three in Table 1). Schubert also confirmed that the vertical structure of the disturbances tends to become more barotropic as the frequency decreases.

Identifying and assigning names or acronyms to a select group of low-frequency teleconnection patterns is a bit like beginning to recognize a few familiar faces from among a large crowd of people. We are hopeful that, by gaining an understanding the nature and causes of a few select patterns, we will be able to make some inferences about the nature and causes of low-frequency variability in general. However, this approach can be counterproductive if, by focusing on the "familiar faces", we lose sight of the "crowd". In this respect, it is worth noting that monthly mean 500 mb height anomaly maps rarely resemble any single recognized teleconnection pattern or simple combination of patterns; no single pattern explains more than 10% of the variance of the monthly mean 500 mb height field over the Northern Hemisphere; and even the "top ten" patterns, taken together, explain only about half that variance. We are not even sure at this point that linear combinations of anomaly "patterns" is the best way to represent the structure inherent in the low-frequency variability.

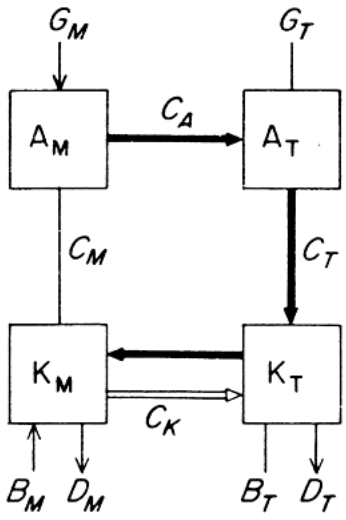

Fig. 46 Schematic illustration of the Lorenz kinetic energy cycle, as adapted to the time mean vs. transient formulation, showing separate arrows for the barotropic energy conversion associated with low and high frequency transients. After Simmons et al. (1983).

References

Andrews, D.G., 1983: A conservation law for small amplitude, quasi-geostrophic disturbances in a zonally asymmetric basic flow. *J. Atmos Sci*, **40**, 85-90.

Barnett, TP., 1983: Interaction between the monsoon and Pacific Trade Wind System at interannual time scales. Part I: the equatorial zone. *Mon. Wea. Rev.*, **111**, 756-773.

Barnston A. and R.E. Livezey, 1987: Classification, seasonality and persistence of low-frequency circulation patterns. *Mon. Wea. Rev.*, **115**, 1083-1126.

Bengtsson, L. and J. Shukla, 1988: Integration of space and in situ observations to study global change. *Amer. Met. Soc. Bull.*, to appear.

Berlage, H.P., 1957: Fluctuations in the general atmospheric circulation of more than one year, their nature and prognostic value. *K. Ned. Meteor. Inst. Meded. Verh.*, **69**, 152pp.

Bjerknes, J., 1964: Atlantic air-sea interaction. *Adv. in Geophys*, ??, 1-82.

_____, 1966: A possible response of the atmospheric Hadley circulation to equatorial anomalies of ocean temperatures, *Tellus*, **18**, 820-829.

_____, Atmospheric teleconnections from the equatorial Pacific, *Mon. Wea. Rev.*,**97**, 163-172.

Blackmon, M. L., 1976: A climatological spectral spectral study of the geopotential height of the Northern Hemisphere. *J. Atmos. Sci.*, **33**, 1607-1623.

_____ and N. -C. Lau, 1980: Regional characteristics of the Northern Hemisphere wintertime circulation: A comparison of the simulation of a GFDL general circulation model with observations. *J. Atmos. Sci.*, **37**, 497-514.

_____., Y.-H. Lee, and J. M. Wallace, 1984a: Horizontal structure of 500 mb height fluctuations with long, intermediate and short time scales. *J. Atmos. Sci.*, **41**, 961-979.

_____, Y.-H. Lee, J. M. Wallace, and H.-H. Hsu, 1984b: Time variations of 500 mb height fluctuations with long, intermediate, and short time scales as deduced from lag-correlation statistics. *J. Atmos. Sci.*, **41**, 981-991.

_____, S.L. Mullen, and G.T. Bates, 1986: The climatology of blocking events in a perpetual January simulation of a spectral general circulation model. *J. Atmos. Sci.*, **43**, 1379-1405.

_____, R. A. Madden, J. M. Wallace, and D. S. Gutzler, 1979: Geographical variations in the vertical structure of geopotential height fluctuations. *J. Atmos. Sci.*, **36**, 2450-2466.

_____, J. M. Wallace, N.-C. Lau, and S. L. Mullen, 1977: An observational study of the Northern Hemisphere wintertime circulation. *J. Atmos. Sci.*, **34**, 1040-1053.

Branstator,G.W., 1985: Analysis of general circulation model sea surface temperature anomaly simulations using a linear model. *J. Atmos. Sci.*, **42**, 2225-2254.

_____, 1987: A striking example of the atmosphere's leading traveling pattern. *J. Atmos. Sci.*, **44**, 2310-2323.

Chang, F.-C. and J.M. Wallace, 1987: Meteorological conditions during heat waves and droughts in the United States Great Plains. *Mon. Wea. Rev.*, **115**, 1254-1269.

Charney, J.G., 1971: Geostrophic turbulence. *J. Atmos. Sci.*, **28**, 1087-1095.

_____, and P. G. Drazin, 1961: Propagation of planetary waves from the lower into the upper atmosphere. *J. Geophys. Res.*, **66**, 83-110.

_____, and DeVore, J.G., 1979: Multiple flow equilibria in the atmosphere and blocking. *J. Atmos. Sci.*, **36**, 1205-1216.

Davis, R., 1978: Predictability of sea-surface temperature anomalies over the North Pacific Ocean. *J. Phys. Oceanogr.*, **8**, 233-246.

Deser, C. and J.M. Wallace, 1987: El Niño events and their relation to the Southern Oscillation. *J. Geophys. Res.*, **92**, 14189-14196.

Dole, R.M., 1983: Persistent anomalies of the extratropical Northern Hemisphere wintertime circulation. In *Large-Scale Dynamical Processes in the Atmosphere*, B.J. Hoskins and R.P. Pearce, Eds., Academic Press, London, 95-109.

_____, 1986a: The life cycles of persistent anomalies and blocking over the North Pacific. *Adv. in Geophys.*, **29**, 31-69.

_____, 1986b: Persistent anomalies of the extratropical Northern Hemisphere wintertime circulation: Structure.. *Mon. Wea. Rev.*, **114**, 178-207.

_____, and N.D. Gordon, 1983: Persistent anomalies of the extratropical Northern Hemisphere wintertime circulation: Geographical distribution and regional persistence characteristics. *Mon. Wea. Rev.*, **111**, 1567-1586.

Edmon, H.J., B.J. Hoskins and M.E. McIntyre, 1980: Eliassen-Palm cross sections for the troposphere. *J. Atmos. Sci.*, **37**, 2600-2616; **38**, 1115.

Esbensen, S. K., 1984: A comparison of intermonthly and interannual teleconnections in the 700 mb geopotential height field during the Northern Hemisphere winter. *Mon. Wea. Rev.*, **112**, 2016-2032.

Fjortoft, R., 1950: Application of integral theorems in deriving criteria of stability for laminar flows and for the baroclinic circular vortex. *Geofysiske Publikasjoner*, **17** No. 6, 52pp.

Fletcher, J.O., R.J. Slutz and S.D. Woodruff, 1983: Towards a comprehensive ocean atmosphere data set. *Tropical Ocean-Atmos. Newsl. (TO-AN)*, **20**, 13-14.

Frankignoul, C., 1985: Sea surface temperature anomalies, planetary waves, and air-sea feedback in the middle latitudes. *Rev. Geophys.*, **23**, 357-390.

_____ and K. Hasselmann, 1977: Stochastic climate models II, Application to sea-surface temperature variability and thermocline variability. *Tellus*, **29**, 284-305.

Frederiksen, J. S., 1979a: The effect of planetary waves on the regions of cyclogenesis: Linear theory. *J. Atmos. Sci.*, **36**, 195-204.

_____, 1978b: Baroclinic instability of zonal flows and planetary waves in multi-level models on a sphere. . *Atmos. Sci.*, **36**, 2320-2335.

_____, 1983: Disturbances and eddy fluxes in Northern Hemosphere flows: Instability of three-dimensional January and July flows. *Atmos. Sci.*, **40**, 836-855.

Geisler, J.E., M.L. Blackmon, G.T. Bates and S. Muñoz, 1985: Sensitivity of January climate response to the magnitude and position of equatorial Pacific sea-surface temperature anomalies. *J. Atmos. Sci.*, **42**, 1037-1049.

Grose, W. L., and B. J. Hoskins, 1979: On the influence of orography on the large scale atmospheric flow. *J. Atmos. Sci.*, **36**, 223-234.

Halem, M., J. Shukla, Y. Mintz, M.-F. Wu, R. Godbole, G. Herman and Y. Sud, 1980: Climate comparisons of a winter and summer simulation with the GLAS general circulation model. *GARP Publ. Series*, **22**, 207-253.

Hannoschöck, G. and C. Frankignoul, 1985: Multivariate statistic analysis of a sea-surface temperature anomaly experiment with the GISS general circulation model. *J. Atmos. Sci.*, **42**, 1430-1450.

Hastenrath, S. and Heller, 1977: On the modes of tropical circulation and climate anomalies. *Quart. J. Roy. Met. Soc.*, **103**, 77-92.

Hayashi, Y. Y., and A. Sumi, 1986: The 30-40 day oscillation simulated in an aqua-planet model. *J. Met. Soc. Japan*, **64**, 451-466.

Held, I.M., 1983: Stationary and quasistationary eddies in the extratropical troposphere: theory. In *Large-Scale Dynamical Processes in the Atmosphere*, B.J. Hoskins and R.P. Pearce, Eds., Academic Press, London, 127-168.

_____ and B.J. Hoskins, 1985: Large-scale eddies and the general circulation of the troposphere. In *Issues in Atmospheric and Oceanic Modeling, Part A: Climate Dynamics*, S. Manabe, Ed., *Adv. in Geophys*, **28**, 3-31,

Hendon, H.H. and D.L. Hartmann, 1982: Stationary waves on a sphere: Sensitivity to thermal feedback. *J. Atmos. Sci.*, **39**, 1906-1920.

Herman, G F. and W.T. Johnson, 1978: The sensitivity of the general circulation to Arctic sea-ice boundaries. *Mon. Wea. Rev.*, **106**, 1649-1664.

_____ and _____, 1985: Variability in a nonlinear model of the atmosphere with zonally symmetric forcing. *J. Atmos. Sci.*, **42**, 2783-2797.

Holopainen, E.O., 1982:Long term budget of zonal momentum in the free atmosphere over Europe in winter. *Quart. J. Roy. Met. Soc.*, **108**, 95-102.

Holton, J. R., 1979: *An Introduction to Dynamic Meteorology*, Academic Press, New York.

Horel, J. D., 1981: A rotated principal component analysis of the interannual variability of the Northern Hemisphere 500 mb height field. *Mon. Wea. Rev.*, **109**, 2080-2092.

_____, and J.M. Wallace, 1981: Planetary scale atmospheric phenomena associated with the Southern Oscillation. *Mon. Wea Rev.*, **109**, 813-829.

Hoskins, B. J., 1978, Horizontal wave propagation on the sphere. In *The General Circulation*, M.L. Blackmon, ed., pp. 144-153. Summer Colloquium Notes, NCAR.

_____, 1983: Dynamical processes in the atmosphere and the use of models. *Quart. J. Roy. Meteor. Soc.*, **109**, 1-21.

_____, I. N. James, and G. H. White, 1983: The shape, propagation and mean-flow interaction of large-scale weather systems. *J. Atmos. Sci.*, **40**, 1595-1612.

_____, and D.J. Karoly, 1981: The steady-state linear response of a spherical atmosphere to thermal and orographic forcing. *J. Atmos. Sci.*, **38**, 1175-1196.

_____, A. J. Simmons, and D. G. Andrews, 1977: Energy dispersion in a barotropic atmosphere. *Quart. J. Roy. Meteor. Soc.*, **103**, 553-567.

Hsu, H.-H., 1987: Propagation of low-level circulation features in the vicinity of mountain ranges. *Mon. Wea. Rev.*, **115**, 1864-1892.

_____, and J.M. Wallace, 1985: Vertical structure of wintertime teleconnection patterns. *J. Atmos. Sci.*, **42**, 1693-1710.

Julian, P.R. and R.M. Chervin, 1978: A study of the Southern Oscillation and Walker Circulation phenomenon. *J. Atmos. Sci.*, **106**, 1433-1451.

Karoly, D, 1985: An atmospheric climatology of the southern hemisphere based on ten years of daily numerical analyses (1972-82): II Standing wave climatology. *Aust. Met. Mag.*, **33**, 105-116.

Kushnir, Y., 1987: Retrograding wintertime low-frequency disturbances over the North Pacific Ocean. *J. Atmos. Sci.*, **44**, 2727-2742.

_____and S. Esbensen, 1986: Northern Hemisphere wintertime variability in a two-level general circulation model. *J. Atmos. Sci.*, **43**, 2968-2998.

Lanzante, J.R., 1984: A rotated eigenanalysis of the correlation between 700 mb heights and sea-surface temperatures in the Pacific and Atlantic. *Mon. Wea. Rev.*, **112**, 2270-2280.

Lau, K.-M and P.H. Chan, 1986: The 40-50 day oscillation and the El Niño/Southern Oscillation: a new perspective. *Bulletin, A. M. S.*, **67**, 533-534.

Lau, N.C., 1981: A diagnostic study of recurrent meteorological anomalies appearing in a 15 year simulation with a GFDL general circulation model. *Mon. Wea Rev.*, **109**, 2287-2311.

Lau, N.-C., 1985: Modeling the seasonal dependence of the atmospheric response to observed El Niños in 1962-76. *Mon. Wea. Rev*, **113**, 1970-1996.

_____, 1988: Variability of the observed midlatitude stormtracks in relation to low-frequency changes in the circulation pattern. *J. Atmos Sci.*, **45**, in press.

_____, and E. O. Holopainen, 1984: Transient eddy forcing of the time-mean flow as identified by quasi-geostrophic tendencies. *J. Atmos.* Sci., **41**, 313-328.

_____ and K.-M. Lau, 1986: The structure and propagation of intraseasonal oscillations appearing in a GFDL general circulation model. *J. Atmos. Sci.*, **43**, 2023-2047.

_____ and A.H. Oort, 1981, 1982: A comparative study of observed Northern Hemisphere general circulation statistics based on GFDL and NMC analyses. Part I: The time mean fields, and Part II: Transient eddy statistics and the energy cycle. *Mon. Wea Rev.*, **109**, 1380-1403 and **110**, 889-906.

Liebmann, B., 1987: Observed relationships between large-scale tropical convection and the tropical circulation on subseasonal time scales. *J. Atmos. Sci.*, **44**, 2543-2561.

_____ and D.L. Hartmann, 1981: Interannual variations of outgoing IR associated with tropical circulation changes during 1974-78. *J. Atmos. Sci.*, **39**, 1153-1162.

Lorenz, E. N., 1955: Available potential energy and the maintenance of the general circulation. *Tellus*, **7**, 157-167.

_____, 1982: Atmospheric predictability experiments with a large numerical model. *Tellus*, **34**, 505-513.

MacVean, M.K., 1985: Longwave growth by baroclinic processes. *J Atmos. Sci.*, **42**, 1089-1101.

Madden, R.A. and P.R. Julian, 1972: Description of global scale circulation cells in the tropics with a 40-50 day period. *J. Atmos. Sci.*, **29**, 1109-1123.

Manabe, S. and T.B. Terpstra, 1974: The effects of mountains on the general circulation of the atmosphere as identified by numerical experiments. *J. Atmos. Sci.*, **31**, 3-42.

Mass, C.F., H.J. Edmon, H.R. Friedman, N.R. Cheeney and E. E. Recker, 1987: The use of compact discs for the storage of large meteorological and oceanographic data sets. *Bulletin of the Amer. Met. Soc.*, **68**, 1556-1558.

Miyakoda, K, J. Sirutis and J. Ploshay, 1987: One month forecast experiments— without anomaly boundary forcings. *Mon. Wea. Rev.*, **114**, 2363-2401.

Mo, K.C., and G.H. White, 1985: Teleconnections in the Southern Hemisphere. *Mon Wea Rev.*, **113**, 22-37.

Mooley, D.A. and J. Shukla, 1987: Variability and forecasting of summer monsoon rainfall over India. In *Revirews of Monsoon Meteorology*, T.N. Krishnamurti and C.-P. Chang, Eds. Oxford University Press, .26-59.

Moura, A.D. and J. Shukla, 1981: On the dynamics of droughts in Northeast Brazil: observations, theory, and numerical experiments with a general circulation model. *J. Atmos. Sci.*, **38**, 2653-2675.

Mullen S.L., 1986: The local balances of vorticity and heat for blocking anticyclones in a spectral general circulation model. *J. Atmos. Sci*, **43**, 1406-1441.

Mysak, L., 1980: Recent advances in shelf wave dynamics. *Rev. Geophys. & Space Phys.*, **18**, 211-241.

Nakamura, H., M. Tanaka and J.M. Wallace, 1987:Horizontal structure and energetics of Northern Hemisphere wintertime teleconnection patterns. *J. Atmos. Sci.*, **44**, 3377-3391.

Namias, J., 1934-82 (Collected Works): *Short Period Climatic Variations.* University of California at San Diego, in three volumes.

_____, 1955: Some meteorological aspects of drought with special reference to the summers of 1952-54 over the United States. *Mon. Wea. Rev.*, **83** 199-205.

_____, 1972a: Space scales of sea-surface temperature patterns and their causes. *Fisheries Bull.*, **70**, 611-617.

_____, 1972b: Influence of Northern Hemisphere general circulation on Northeast Brazil drought. *Tellus*, **24**, 336-343.

_____, 1978: Multiple causes of the North American abnormal winter 1976-77. *Mon Wea Rev.*, **106**, 279-295.

Newton, C.W., 1956: Mechanisms of circulation change during a lee cyclogenesis. *J. Meteorol.*, **13**, 528-539.

Nigam, S., I.M. Held and S. W. Lyons, 1986: Linear simulation of the stationary eddies in a general circulation model. Part I: The No-Mountain model. *J. Atmos. Sci*, **43**, 2944-2961.

Palmer, T.N., 1988: Medium and extended range prediction and stability of the PNA mode. *Quart. J. Roy. Met. Soc.*, in press.

_____, and D.A. Mansfield, 1986: A study of wintertime circulation anomalies during past El Niño events, using a high-resolution general circulation model. *Quart J. Roy. Met. Soc.*, **112**, 613-660.

_____, G.J. Shutts and R. Swinbank, 1986: Alleviation of a systematic westerly bias in general circulation and numerical weather prediction models through an orographic wave drag. *Quart. J. Roy. Met. Soc.*, **112**, 1001-1039.

_____, and Z. Sun, 1985: A modeling and observational study of the relationship between sea-surface temperature in the northwest Atlantic and the atmospheric general circulation. *Quart. J. Roy. Met. Soc.*, **111**, 947-975.

Petterssen, S., 1956: *Weather Analysis and Forecasting.* Volume 1, 2nd Ed., McGraw-Hill, 422pp.

Physick, W.L., 1981: Winter depression tracks and climatological jet streams in the Southern Hemisphere during the FGGE Year. *Quart. J Roy. Met. Soc.*, **107**, 883-898.

Pitcher, E.J., R.C. Malone, V. Ramanathan, M.L. Blackmon, K. Puri, and W. Bourke., 1983: January and July simulations with a spectral general circulation model. *J. Atmos. Sci.*, **40**, 580-604.

_____, M.L. Blackmon, G. Bates and S. Muñoz, 1988: The effect of North Pacific sea-surface temperature anomalies on the January climate of a general circulation model. *J. Atmos. Sci.*, **45**, in press.

Plumb, A.R., 1985: An alternative form of Andrews' conservation law for quasi-geostrophic waves on a steady, nonuniform flow. *J. Atmos. Sci.*, **42**, 298-300.

_____, 1986: Three-dimensional propagation of transient quasi-geostrophic eddies and its relation with the eddy forcing of the time-mean flow. *J. Atmos. Sci.*, **43**, 1657-1670.

Prohaska, J., 1976: A technique for analyzing the linear relationships between two meteorological fields. *Mon. Wea. Rev.*, **104**, 1345-1353.

Rasmusson, E.M., 1968: Atmospheric water vapor transport and the water balance of North America. Part II: Large-scale water balance investigations. *Mon. Wea. Rev.*, **96**, 720-734.

_____ and T. Carpenter, 1982: Variations in tropical sea-surface temperature and surface wind fields associated with the Southern Oscillation/El Niño. *Mon. Wea. Rev.*,**110**, 354-384.

_____ and _____, 1983: the relationship between eastern equatorial Pacific sea-surface temperatures and rainfall over India and Sri Lanka. *Mon. Wea. Rev.*, **111**, 517-528.

Shukla, J. and J.M. Wallace, 1983: Meteorological aspects of the El Niño/Southern Oscillation. *Science*, **222**, 1195-1202.

Ratcliffe, R.A.S. and R Murray, 1970: New lag associations between North Atlantic sea-surface temperature and European pressure applied to long-range weather forecasting. *Quart. J. Roy. Met. Soc.*, **96**, 226-246.

Rex, D., 1950: Blocking action in the middle troposphere and its effect on regional climate. *Tellus*, **2**, 196-211, 275-301.

Rhines, P.B., 1970: Edge-, bottom-, and Rossby waves in a rotating stratified fluid. *Geophys. Fluid Dyn.*, **1**, 273-303.-

_____, 1975: Waves and turbulence on a β-plane. *J. Fluid Mech.*, **69**, 417-443.

Rogers, J. C., 1981: The North Pacific Oscillation. *J. Climatol.*, **1**, 39-57.

Rowntree, P.R., 1972: The influence of tropical east Pacific ocean temperatures on the atmosphere. *Quart. J. Roy. Met. Soc.*, **98**, 290-321.

_____, 1976: Response of the atmosphere to a tropical Atlantic ocean temperature anomaly. *Quart. J. Roy. Met. Soc.*, **102**, 607-625.

Salby, M., 1982: A ubiquitous wavenumber 5 anomaly in the Southern Hemisphere during FGGE. *Mon Wea. Rev.*, **110**, 1712-1720.

Sardeshmukh, P.D, and B.J. Hoskins, 1988: On the generation of global rotational flow by steady, idealized tropical divergence. *J. Atmos. Sci.*, **45**, to appear.

Sawyer, J.S., 1970: Observational characteristics of atmospheric fluctuations with a time scale of a month. *Quart. J. Roy. Met. Soc.*, **96**, 610-625.

Schubert, S.D., 1986: The structure, energetics and evolution of the dominant frequency-dependent three-dimensional atmospheric modes. *J. Atmos. Sci.*, **43**, 1210-1237.

Sellers, W.D., 1965: *Physical Climatology*. University of Chicago Press, Chicago, p.112.

Shukla, J. 1981: Dynamical predictability of monthly means. *J. Atmos. Sci.*, **38**, 2547-2572.

_____ and Y. Mintz, 1982: The influence of land-surface evaporation on the earth's climate. *Science*, **215**, 1498-1501.

_____, and D.A. Paolino, 1983: The Southern Oscillation and long-range forecasting of the summer monsoon rainfall over India. *Mon. Wea. Rev.*, **111**, 1830-1837.

_____ and J.M. Wallace, 1983: Numerical simulation of the atmospheric response to equatorial Pacific sea-surface temperature anomalies. *J. Atmos. Sci.*, **40**, 1613-1630.

Shutts, G.J., 1983: The propagation of eddies in diffluent jetstreams: Eddy vorticity forcing of blocking flow fields. *Quart. J. Roy. Met. Soc.*, **109**, 737-761.

_____, 1986: A case study of eddy forcing during an Atlantic blocking episode. *Adv. in Geophys.*, **29**, 135-164.

Simmons, A.J., 1982: The forcing of planetary wave motion by tropical diabatic heating. *Quart. J. R. Meteorol. Soc.*, **108**, 503-534.

_____, J.M. Wallace and G.W. Branstator, 1983: Barotropic wave propagation and instability, and atmospheric teleconnection patterns. *J. Atmos. Sci.*,**40**, 1363-1392.

_____, and B.J. Hoskins, 1978: The life cycles of some nonlinear baroclinic waves. *J. Atmos. Sci.*, **35**, 414-432.

Starr, V.P., 1948: An essay on the general circulation of the earth's atmosphere. *J. Meteorol.*, **15**, 271-277.

Sutera, A, 1986: Probability density distribution of large-scale atmospheric flow. *Adv. in Geophys.*, **29**, Academic Press, 227-249.

Trenberth, K.E., 1979, Interannual variability of the 500 mb zonal mean flow in the Southern Hemisphere. *Mon Wea. Rev.*, **107**, 1515-1524.

_____, 1980: Planetary waves at 500 mb in the Southern Hemisphere. *Mon Wea Rev.*, **108**, 1378-1389.

_____, 1981a: Observed Southern Hemisphere eddy statistics at 500 mb: Frequency and spatial dependence. *J. Atmos. Sci.*, **38**, 2585-2605.

_____, 1981b: Interannual variability of the Southern Hemisphere flow: Regional characteristics. *Mon Wea. Rev.*, **108**, 127-136.

_____, 1982: Seasonality in Southern Hemisphere eddy statistics. *J Atmos. Sci*, **39**, 2507-2520.

_____, 1986: An assessment of the impact of transient eddies on the zonal flow during a blocking episode using localized Eliassen-Palm flux diagnostics. *J. Atmos. Sci.*, **43**, 2070-2087.

_____, 1987: The zonal mean westerlies over the Southern Hemisphere. *Mon Wea. Rev.*, **115**, 1528-1533.

_____ and K.C. Mo, 1985: Blocking in the Southern Hemisphere. *Mon Wea. Rev.*, **113**, 3-21.

_____, and D.J. Shea, 1987: On the evolution of the Southern Oscillation, *Mon. Wea Rev.*, **115**, 3078-3096.

Troup, A.J., 1965: The Southern Oscillation. *Quart J. Roy. Met. Soc.*, **91**, 490-506.

van Loon, H., and J. C. Rogers, 1978: The seesaw in winter temperatures between Greenland and northern Europe. Part I: General description. *Mon. Wea. Rev.*, **106**, 296-310.

Walker, G.T. and E.W. Bliss, 1932: World Weather V. *Mem. R. Met. Soc.*, **4**, 53-84.

Walker, J. and P. R. Rowntree, 1977: The effect of soil moisture and rainfall on the circulation and rainfall in a tropical model. *Quart. J. Roy. Met, Soc.*, **103**, 29-46.

Wallace, J. M., 1983: The climatological mean stationary waves: Observational evidence. In *Large-Scale Dynamical Processes in the Atmosphere*, B.J. Hoskins and R.P. Pearce, Eds., Academic Press, London, 27-53.

_____ and M.L. Blackmon, 1983: Observations of low-frequency atmospheric variability. In *Large-Scale Dynamical Processes in the Atmosphere*, B.J. Hoskins and R.P. Pearce, Eds., Academic Press, London, 55-94.

_____, and D. S. Gutzler, 1981: Teleconnections in the geopotential height field during the Northern Hemisphere winter. *Mon. Wea. Rev.*, **109**, 785-812.

_____, and H.-H. Hsu, 1983: Ultra-long waves and two-dimensional Rossby waves. *J. Atmos. Sci.*, **40**, 2211-2219.

_____ and Q. Jiang, 1987: On the observed structure of the interannual variability of the atmosphere/ocean climate system. In *Atmospheric and Oceanic Variability*, H. Cattle, ed., Roy. Met. Soc., Bracknell, Berks, xx.

_____, and N.-C. Lau, 1985: On the role of barotropic energy conversions in the general circulation. Atmospheric and Oceanic Modeling, a volume in *Advances in Geophysics*, **28**, 33-74.

_____, G-H. Lim and M.L. Blackmon,1988: On the relationship between cyclone tracks, anticyclone tracks and baroclinic waveguides. *J. Atmos. Sci..*, **44**, in press.

_____, S. Tibaldi and A.J. Simmons, 1983: Reduction of systematic forecast error in the ECMWF model through the introduction of an envelope orography. *Q.J.Roy. Meteorol. Soc.*, **109**, 683-717.

Walsh, J.E. , 1986: Diagnostic studies of large-scale air-sea-ice interactions. In *The Geophysics of Sea Ice*, N. Untersteiner, Ed., Plenum Press, New York. 755-784.

Walsh, J.E. and C.M. Johnson, 1979: Interannual atmospheric variability associated with fluctuations in Arctic sea-ice extent. *J. Geophys. Res.*, **84**, 6915-6928.

Walsh, J.E. and J.E. Sater, 1981: Monthly and seasonal variability in the atmosphere-ocean-ice systems of the North Pacific and the North Atlantic. *J. Geophys. Res.*,**86C**, 7425-7445.

_____ and Richman, 1981: Seasonality in the associations between surface temperatures over the United States and the North Pacific Ocean. *Mon. Wea. Rev.*, **109**, 767-783.

Weare, B., 1977: Empirical orthogonal analysis of Atlantic sea-surface temperatures. *Quart. J. Roy. Met. Soc.*, **103**, 467-478.

Weare, B., A. Navato and R.E. Newell, 1976: Empirical orthogonal analysis of Pacific Ocean sea surface temperatures. *J. Phys. Oceanogr.*, **6**, 671-678.

Webster, P.J. and H.R. Chang, 1988: Energy accummulation and emanation regions in low latitudes: Impacts of a zonally varying basic state. *J. Atmos. Sci.*, **45**, to appear.

Weickmann K.M., G.R. Lussky, and J.E. Kutzbach, 1985: Intraseasonal (30-60-day) fluctuations of outgoing longwave radiation and 250 mb streamfunction during northern winter. *Mon. Wea. Rev.*, **113**, 941-961.